

Testing the chemical homogeneity of chemically-tagged dissolved birth clusters

Chloe M. Cheng,¹★ Natalie Price-Jones,^{1,2} and Jo Bovy^{1,2}

¹Department of Astronomy and Astrophysics, University of Toronto, 50 St. George Street, Toronto, ON, M5S 3H4, Canada

²Dunlap Institute for Astronomy and Astrophysics, University of Toronto, 50 St. George Street, Toronto, ON, M5S 3H4, Canada

Accepted XXX. Received YYY; in original form ZZZ

ABSTRACT

Chemically tagging stars back to common formation sites in the Milky Way and establishing a high level of chemical homogeneity in these chemically-tagged birth clusters is important for understanding the chemical and dynamical history of the Galactic disc. We constrain the intrinsic abundance scatter in 17 newly chemically-tagged dissolved birth clusters found in the APOGEE survey by modeling APOGEE spectra as a one-dimensional function of initial stellar mass, performing forward modeling of the observed stellar spectra, and comparing the data and simulations using Approximate Bayesian Computation. We test this method on the well-known open clusters M67, NGC 6819, NGC 7789, and NGC 6791. We study 15 elements in APOGEE and find that, in general, we are able to obtain very strong constraints on the intrinsic abundance scatter of most elements in the chemically-tagged birth clusters, with upper limits of $\lesssim 0.02$ dex for C, $\lesssim 0.03$ dex for O, Mn, and Fe, $\lesssim 0.04$ dex for Si and Ni, and $\lesssim 0.05$ dex for N, Mg, and Ca. While we find some evidence for a small amount of chemical inhomogeneity in the remaining elements (i.e. Na, Al, S, K, Ti, and V), we are still able to obtain stronger limits compared to those found for open clusters, consistent with previous findings. By strongly constraining the level of chemical homogeneity within reconstructed birth clusters, we can strengthen the statement that these groups of stars represent birth clusters, with promising implications for future chemical tagging studies.

Key words: methods: data analysis — stars: abundances — stars: statistics — Galaxy: abundances — Galaxy: evolution — Galaxy: structure

1 INTRODUCTION

Uncovering the history of the Galactic disc is a fundamental problem in astrophysics, and understanding its formation as a principal stellar component of the Milky Way is a crucial goal in the theory of galaxy formation. An intimate knowledge of the chemical and dynamical history of the disc can allow us to understand other crucial processes in stellar and galaxy formation, such as chemical enrichment processes and the star formation history, at a high level of detail. This perspective about the history of the Galaxy will give us greater insight into where it is today and where it will be in the future, and knowing about our own Galaxy will help us to understand the wider Universe around us. However, it is difficult to achieve this understanding of the formation history of the disc due to the fact that the stars, gas, and dust in the disc are highly dissipated in comparison to other stellar structures, like the halo or the bulge, and much of its chemical and dynamical information has been lost during the period of dissipation that led to the formation of the disc as we see it today (Freeman & Bland-Hawthorn 2002).

As such, a major goal of near-field cosmology is to reconstruct

components of the disc that were gravitationally associated with each other before this dissipation occurred. A specific example is the reconstruction of birth clusters, the progenitors of star clusters. Star clusters are born from giant molecular clouds (GMCs), in strongly self-gravitating cores of molecular gas (Lada & Lada 2003), and are thought to emerge as birth clusters in the collapse of their progenitor clouds (Freeman & Bland-Hawthorn 2002). The majority of birth clusters are subsequently dispersed into the disc over a relatively short period of time, with very few remaining gravitationally bound as the star clusters that we see today (Lada & Lada 2003). Thus, the ability to reconstruct many birth clusters over the entire age of the Galaxy would illuminate key information about the chemical and dynamical evolution of the disc. For example, this would allow for the determination of accurate ages for stellar groups (Freeman & Bland-Hawthorn 2002), the reconstruction of the stellar cluster mass function (or the relative distribution of initial star cluster masses), and the constraining of radial migration models, to track the manner in which stars have been displaced from their initial radial positions due to interactions with the spiral and bar structures (Ting et al. 2015; Price-Jones et al. 2020).

A technique by which we can attempt to reconstruct birth clusters is that of chemical tagging, which makes use of the immense

★ E-mail: cmtcheng@uwaterloo.ca (CC)

amount of historical information that is available in the chemistry of stars in the disc. We can use this technique to attempt to identify birth clusters by associating (or ‘tagging’) a large sample of stars with their precise time and site of formation. In other words, we would like to be able to identify birth clusters by grouping stars with similar chemistry, in the hopes that these associations represent common formation sites (Freeman & Bland-Hawthorn 2002).

However, the ability to use chemical tagging techniques presupposes the chemical homogeneity of birth clusters. Chemical homogeneity requires that birth clusters have negligible abundance variations at the time of their formation (Freeman & Bland-Hawthorn 2002). This could be possible through two mechanisms: either the GMC in which a birth cluster’s member stars formed was uniformly mixed in several chemical elements before any stars began to form, or a small number of high mass stars formed early in the life of the GMC and enriched the cloud uniformly (Quillen 2002). As such, older stars associated with the same birth cluster should have some identical elemental abundances (Freeman & Bland-Hawthorn 2002). Abundance variations among birth cluster members can occur at later stages of stellar evolution due to internal mixing, however this mixing should only affect lighter elements that are subsequently synthesized within the stars, whereas the abundances of heavier elements should remain at or near their initial levels (De Silva et al. 2009). Without some level of initial chemical homogeneity, however, it would not be possible to tag stars that have been dispersed into the disc back to common formation sites (Freeman & Bland-Hawthorn 2002). It stands to reason that birth clusters should be relatively homogeneous, since the regions in which they form in GMCs are highly turbulent and well-mixed (McKee & Tan 2002). Turbulent mixing has been shown to produce homogeneous star clusters from GMCs in simulations by Feng & Krumholz (2014), but finding birth clusters in our Galaxy via chemical tagging and proving that they are truly homogeneous is still a widely explored area.

Several studies have already been completed on the topic of chemical homogeneity, using various samples of open clusters. Open clusters represent a very small proportion of birth clusters that remain gravitationally bound into the present day (Allen et al. 2006). Open clusters are useful for chemical homogeneity studies because they consist of a group of stars that were born in the same place as the disc but have managed to remain gravitationally bound over a longer period of time, and thus represent a sample of the early Galactic disc (Freeman & Bland-Hawthorn 2002). If it can be shown that open clusters that have remained bound into present day are chemically homogeneous, then it is likely that dispersed birth clusters are chemically homogeneous as well, paving the way for chemical tagging.

Some studies have found inhomogeneity in open clusters; for example, Liu et al. (2016) studied several elements in 16 stars in the Hyades and found that the Hyades is chemically inhomogeneous at the 0.02 dex level. Spina et al. (2018) studied five stars in the Pleiades and found chemical variations that they attributed to planet engulfment events and the evolution of planetary systems.

However, other studies have found that these inhomogeneities are limited to comparisons across evolutionary stage, or are so small as to be below measurement uncertainties. For example, Blanco-Cuaresma et al. (2014) examined 31 open clusters and found that stars at different stages of stellar evolution are chemically inhomogeneous relative to each other, in that they have different chemical abundance patterns. This may be the result of processes such as NLTE effects, atomic diffusion, mixing, and systematic biases. In a study on M67, Souto et al. (2018) studied several different classes of

stars, and while they found chemical homogeneity within each evolutionary stage, they found significant variations in chemical abundances across different stages. They attribute these inhomogeneities to chemical diffusion. Souto et al. (2019) also studied member stars of M67 and found significant abundance variations between stars as a function of stellar mass/position on the Hertzsprung-Russell diagram, attributing these differences to atomic diffusion. Similarly, Liu et al. (2019) concluded that while M67 was likely born homogeneous, certain subsets of its members, such as turn-off stars, may be inhomogeneous today due to atomic diffusion. As such, turn-off stars are not good candidates for chemical tagging. Casamiquela et al. (2020) examined the open clusters Ruprecht 147, the Hyades, and Praesepe and found certain levels of inhomogeneity in each cluster, but despite this they found that it is still possible to distinguish each cluster’s chemical signature.

Additionally, some studies show that the level of chemical homogeneity within an open cluster is below the level of state-of-the-art measurement uncertainties. De Silva et al. (2006) analyzed several heavy elements in dwarf stars in the Hyades, and their results implied that there is little to no intrinsic scatter between cluster members. De Silva et al. (2007) analyzed several elements in twelve red giant stars of Collinder 261 and estimated the intrinsic scatter to be < 0.05 dex, with these high levels of homogeneity indicating the preservation of chemical information in this cluster. Pancino et al. (2010) analyzed three red clump stars in five open clusters and found that the abundance patterns of these stars were largely close to solar, and that their [Fe/H] abundances were indicative of chemical homogeneity. Finally, Poovelil et al. (2020) found the clusters they studied to have a level of abundance scatter in most elements indicative of chemical homogeneity. However they found that there is a velocity-dispersion-dependence for chemical homogeneity, implying that massive open clusters should be avoided in chemical tagging studies.

What all of these studies have in common is that they use the traditional method of deriving abundances from stellar spectra and comparing scatter in these derived abundances to the measured uncertainties. However, this method can be complicated due to incomplete theoretical models of stellar surfaces and instrumental observational errors (Ness et al. 2015). To avoid these complications, Bovy (2016) (B16 hereafter) took the less-traditional route of determining tight constraints on the initial abundance spread in open clusters using high-resolution stellar spectra. This method is the approach we utilize for a new assessment of chemical homogeneity in a catalogue of birth clusters that have been identified via chemical tagging by Price-Jones et al. (2020). In particular, we constrain the abundance scatter in chemically-tagged birth clusters using stellar spectra instead of derived abundances, which allows us to report the abundance scatter with a very small uncertainty.

B16 was able to define tight upper limits on the intrinsic abundance scatter of the old open clusters M67, NGC 6819, and NGC 2420 using this method. A combined upper limit of less than 0.05 dex at 95% confidence was found for nearly all elements studied, using data from the 12th data release (DR12, Alam et al. 2015) of the Apache Point Observatory Galactic Evolution Experiment (APOGEE, Majewski et al. 2017, see Section 2.1 for details). We test this method using some of the same clusters as B16 as well as additional old open clusters (described in Section 2.2.2) using APOGEE’s more recent 14th data release (DR14, Abolfathi et al. 2018). What makes our study unique, however, is that we examine several newly blindly chemically-tagged birth clusters, found by Price-Jones et al. (2020) (described in Section 2.2.3). This analysis truly tests the limits of this method and determines whether it is

possible to obtain tight constraints on the intrinsic abundance scatter of the remnants of star clusters that have been scattered across the Galactic disc.

This paper is organized as follows: in Section 2, we review the APOGEE survey from which the data for this study was obtained, we describe the open and chemically-tagged birth clusters that we test and analyze, and we outline some of the data reduction processes that we implement. In Section 3, we detail the Approximate Bayesian Computation method, describe the one-dimensional initial mass model and fitting procedures that we use to characterize the data, and define the process for generating synthetic spectra. We describe the algorithm for inferring the abundance scatter using forward simulations of the data and Approximate Bayesian Computation as well. We present the results in Section 4. We discuss the implications of these results in Section 5, and we present our conclusions in Section 6.

2 DATA

2.1 APOGEE

We analyze spectroscopic data from DR14 (Abolfathi et al. 2018) of the Apache Point Observatory Galactic Evolution Experiment (APOGEE, Majewski et al. 2017), a component of the Sloan Digital Sky Survey IV (SDSS-IV, Blanton et al. 2017). APOGEE is a high-resolution ($R = 22,500$) spectroscopic survey, observing the H band ($1.51 - 1.70\mu\text{m}$) using a 300-fiber spectrograph mounted on the 2.5-metre Sloan Foundation telescope (Gunn et al. 2006), located at the Apache Point Observatory. For each open cluster that we study, we use `apStar` spectra that combine the observations from all APOGEE observations ('visits' in APOGEE nomenclature) of a given star (Holtzman et al. 2015).

2.1.1 Spectral Windows

Associated with APOGEE is the APOGEE Stellar Parameter and Chemical Abundances Pipeline (ASPCAP, García Pérez et al. 2016), a software package for the automated analysis of APOGEE spectra. ASPCAP derives atmospheric parameters and chemical abundances from observed spectra using a χ^2 minimization in a multidimensional parameter space to compare observed spectra to theoretical spectra. We make use of ASPCAP in a variety of ways, but an important aspect of the package to highlight for the context of this work is the spectral windows. ASPCAP uses a set of numbers as a function of wavelength for each element to weight the contribution of different pixels to the $\Delta\chi^2$ used in fitting for the abundance of a particular element. Thus, high weight is given to pixels that are very sensitive to the abundance of the element and relatively insensitive to the abundances of other elements in APOGEE. Essentially, this is equivalent to identifying the positions of the transitions for each element (García Pérez et al. 2016).

Specifically, the derivatives of the model fluxes with respect to each elemental abundance are examined for a star with $T_{\text{eff}} = 4000$ K, $\log g = 1.0$, and three different metallicities ($[\text{M}/\text{H}] = +0.0, -1.0$, and -2.0). If the modulus of the derivative of the model flux at a given wavelength pixel with respect to a certain elemental abundance is greater than 3 times the standard deviation of all of the points in the entire APOGEE spectrum, then this wavelength pixel is assumed to be sensitive to variations in the abundance of the element in question for each metallicity. The weights are normalized to the value of the most sensitive point. If this wavelength is sensitive to

the abundance of another element in APOGEE (except for Fe), the weight of the other element is subtracted. This can result in negative weights, which are unphysical and thus set to zero. All of the weights computed for each metallicity are combined as such:

$$w_{\lambda,i} = 0.3 \times w_{\lambda,i,[\text{M}/\text{H}] = +0.0} \\ + 0.3 \times w_{\lambda,i,[\text{M}/\text{H}] = -1.0} \\ + 0.4 \times w_{\lambda,i,[\text{M}/\text{H}] = -2.0}, \quad (1)$$

which corresponds to Equation (6) in García Pérez et al. (2016), favouring wavelengths that are sensitive to abundance changes at lower metallicity, since variations of the modulus of the derivative are harder to detect here. These weights are further adjusted via a multiplicative factor that adjusts for how well a model spectrum for the star Arcturus reproduces actual observations of Arcturus (Hinkle et al. 1995). A second multiplicative factor is also applied, which adjusts for how well the APOGEE spectra are reproduced by the model fluxes. For more details, see García Pérez et al. (2016).

Our use of the spectral windows represents a key difference in the method used in our study and that outlined in B16, beyond our updating of the method from DR12 to DR14. Since we examine APOGEE DR14 spectra, we use the DR14 windows in our analysis, which contain several changes in the line list when compared to DR12. For example, several new lines were added from NIST and other literature publications, and hyperfine splitting was included for some elements (Holtzman et al. 2018).

We also make several modifications to the weights that we use from the DR14 spectra. First, for the elements C, N, and Fe, we cut several of the smallest non-zero weights from consideration. This is because, between DR12 and DR14, the number of pixels with non-zero weights available for these elements increased by an order of magnitude, due to the additions to the line list described above (the numbers of non-zero weights for the remaining elements are of similar sizes between DR12 and DR14). For example, the number of non-zero weights for C increases from 513 in DR12 to 3800 in DR14, which is concerning since this means that more than half of the pixels in the wavelength range of APOGEE contribute a signal to C. This means that analyzing C using its full set of windows will result in a small amount of signal being picked up from other elements since, despite the efforts of ASPCAP to subtract the contribution of other elements at the same pixel as described above, some contamination still occurs. The increased number of lines also has the effect of increasing our run times significantly. Upon examination of these non-zero weights, we see that a large number of them are extremely small in value, which means that they are unlikely to contribute significantly to our analysis of these elements. In order to avoid contamination from other elements and obtain more reasonable run times for our analysis of C, N, and Fe, we make a cut on the DR14 windows by removing the non-zero weights in DR14 that are smaller than the smallest 70% of the non-zero DR12 weights. This allows us to use the non-zero weights in DR14 that correspond to the strongest non-zero weights in DR12, which helps us keep our method as similar as possible to that developed in B16. We tested various different percentages of the smallest lines to cut, and we found that cutting the smallest 70% of the non-zero DR12 weights provides us with more reasonable run times and numbers of non-zero weights for C, N, and Fe in DR14 that are of comparable size to the set of non-zero weights for these elements in DR12.

The second modification that we make to the windows is related to our use of the POLYNOMIAL SPECTRAL MODELLING (PSM) code (Rix et al. 2016), where we mask elemental weights in DR14 that are

outside of the bounds of the APOGEE detectors used in DR12. This modification is described in detail in Section 3.3.

We make use of 15 elements in APOGEE: C, N, O, Na, Mg, Al, Si, S, K, Ca, Ti, V, Mn, Fe, and Ni.

2.2 The Stellar Sample

2.2.1 Generalities

We test our method with 4 open clusters and use it to analyze 17 chemically-tagged birth clusters, all with large numbers of red giant stars (initially ≥ 10 before the red clump giant removal, described in Section 2.4). We analyze only giant stars in this study, because we only model differences in the chemical absorption line profiles that occur due to temperature and abundance variations. We do not use dwarf stars, for example, because in dwarfs, differences in the initial rotation speeds and inclination angles can give rise to additional line variations. However, in giant stars, rotation speeds are negligible due to magnetic braking (Gray 1982) and the distribution in inclination angles is relatively narrow (de Medeiros et al. 1996). Thus, these rotational effects are typically negligible and can be ignored in giant stars. Red giants themselves are also likely to represent the initial chemical composition of the cluster to which they belong. For example, for stars near the turn-off point, effects like atomic diffusion greatly affect stellar surface abundances (Dotter et al. 2017), causing stars at this particular evolutionary stage to display chemical inhomogeneity. However, as stars evolve from the turn-off point to the sub-giant and red giant branches, the surface convection zones deepen, erasing signatures of diffusion and returning these stellar surface abundances to approximately their primordial values (Liu et al. 2019).

We derive the stellar properties of all stars used using ASTRONN, a neural network designed for high-resolution spectroscopy (Leung & Bovy 2019a). We limit the stars that we use to be in the photometric effective surface temperature range of $4000 \text{ K} \leq T_{\text{eff}} \leq 5000 \text{ K}$, since this range contains most of the stars that are within the clusters that we study, and since spectral modeling becomes more uncertain beyond $T_{\text{eff}} < 4000 \text{ K}$ (B16). All clusters and their respective numbers of red giant members between the T_{eff} limits are listed in Table 1. It should be noted that we remove red clump stars from the clusters we analyze, and the numbers of these red clump stars are also reported in Table 1. More detail on this process is given in Section 2.4.

We obtain our cluster members from two sources. The test open-cluster sample comes from the Open Cluster Chemical Analysis and Mapping (OCCAM, Donor et al. 2018) survey catalogue. The candidate-birth-cluster sample comes from a catalogue of blindly chemically-tagged stars from across the Galactic disc, found in Price-Jones et al. (2020) to make up chemically homogeneous groups. Here we will give a brief summary of each catalogue and how the membership of their clusters was determined.

2.2.2 OCCAM

The OCCAM survey is a comprehensive spectroscopic data set containing information about hundreds of open clusters in the Milky Way, including their Galactic dynamical and chemical parameters (Donor et al. 2018). We test our method for constraining cluster homogeneity on four open clusters using data from the OCCAM survey, including M67 and NGC 6819, which were previously analyzed in B16, as well as NGC 7789 and NGC 6791. These particular

clusters were chosen from the larger sample of OCCAM open clusters since they are the ones with the required number of red giant member stars (≥ 10 as described above) after the T_{eff} cuts. The OCCAM clusters tested and their numbers of members are reported in Table 1.

Open cluster membership was assigned by OCCAM in two ways. Firstly, known members of open clusters that were observed for APOGEE calibration purposes were chosen, where stars with previously measured abundance and/or high quality membership studies based on radial velocity were targeted specifically. Secondly, ‘likely’ cluster targets were chosen, on the basis of their location in the colour-magnitude diagram of the open cluster in question, using colours from 2MASS (Cutri et al. 2003) and WISE (Wright et al. 2010). Membership was then further constrained using Gaia proper motions (Gaia Collaboration et al. 2018). The final OCCAM sample contains giant members as well as potential dwarf members (Donor et al. 2018). In this study, we only make use of the stars that are flagged as giant members, due to the considerations discussed above.

2.2.3 Blindly Chemically-Tagged Birth Clusters

In Price-Jones et al. (2020), the Density-Based Spatial Clustering Applications with Noise algorithm (DBSCAN, Ester et al. 1996) was applied to a subset of ASTRONN abundances that were derived from APOGEE spectroscopic data. DBSCAN identifies groups as overdensities in chemical space; specifically, it evaluates the chemical space around each star and assigns these stars to groups once it is determined whether there is an adequate number of surrounding stars to classify the region as high-density. It is useful for blind applications to a large chemical space because it does not require any assumptions about the number of expected groups. Additionally, it does not assign every star in the sample to a group as it is able to flag certain stars as noise. This is useful because it is expected that many of the stars in APOGEE are the singular representatives of their respective birth clusters, because the sample of stars in APOGEE is small compared to the number of all of the stars in the Galaxy (Price-Jones et al. 2020).

DBSCAN was used to blindly chemically tag an 8-dimensional chemical space in APOGEE, resulting in a catalogue of 21 chemically-tagged groups of stars with more than 15 members. The members of these groups are scattered across the entire sample of stars in APOGEE, with the oldest group having most of its members located at large Galactic latitudes and the youngest group having most of its members located close to the Galactic midplane. These groups were found to be chemically homogeneous in each of the 8 abundances used for chemical tagging, as well as in 7 other well-measured ASTRONN abundances. Members of the groups were also found to be consistent with sharing the same ages, with the ages of the groups ranging from 3-10 Gyr. In addition, it was found that simulated open clusters demonstrated orbital action spreads that were qualitatively similar to the spreads in orbital actions of the chemically-tagged groups. These characteristics led to the belief that these groups represent stellar birth clusters, and studying them could allow us to explore the early Galactic disc and its subsequent evolution at an unprecedented level of detail (Price-Jones et al. 2020).

We analyze 17 of the blindly chemically-tagged birth clusters, henceforth referred to as ‘PJ clusters’ or ‘PJ birth clusters’. The PJ clusters we use and their numbers of members are reported in Table 1. We choose these particular clusters from the larger sample

of PJ clusters since they are the ones with the required number of red giant member stars (≥ 10 as described above).

2.3 Uncertainty and Error Analysis

The spectra in APOGEE have reported individual pixel-level uncertainties which are computed from a noise model that tracks the Poisson photon-counting noise. The correlations between the uncertainties of adjacent pixels are left unrecorded. Theoretically, these uncertainties should characterize the noise in the spectra realistically. However, Nidever et al. (2015) and B16 tested the precision of these reported uncertainties and found that the uncertainties are significantly underestimated in large areas of the spectra (which is likely a result of issues with telluric correction) and also display significant correlations (which is likely a result of the continuum normalization, with perhaps some contribution from scattered light). We therefore apply several corrections to the spectra that we examine and their associated uncertainties in order to account for these issues.

2.3.1 Repeats Residuals

B16 performed a detailed test of the reported APOGEE uncertainties and determined an empirical model for the spectral errors via repeat observations. 1,381 giant stars with 3 repeat observations were selected from the APOGEE DR12 data set, for a total of 4,143 individual spectra. The selected giants had $4000 \text{ K} \leq T_{\text{eff}} \leq 5000 \text{ K}$, $\log g < 3.5$, $10 < H < 11$, each with three one-hour-long exposures. The combined spectra for each star had an average overall signal to noise ratio ($\text{S/N} > 300$) and each individual spectrum had an overall $\text{S/N} > 80$. These criteria for targets were chosen as they were similar to the majority of the open cluster members considered. Each individual exposure spectrum and each combined APOGEE spectrum were continuum-normalized for each target star and the normalized residuals were computed according to the expression

$$\Delta f_{\lambda}^i = \frac{f_{\lambda}^i - f_{\lambda}^i, \text{combined}}{\delta_{\lambda}^i} \quad (2)$$

for each star i , where δ_{λ}^i is the reported uncertainty for each pixel λ . This expression corresponds to Equation (B1) in B16. Pixels with $\text{S/N} < 50$ or corresponding to any bad pixel flags (see Section 2.3.2 for details) were removed from consideration. B16 used these normalized repeat observation residuals as a direct empirical sampling of the noise in the spectra.

In this study, we make use of B16’s repeat observations algorithm to produce 3,150 repeats residuals for 1,050 stars in DR14 of APOGEE. We use these repeats residuals in the same way as B16, as a direct empirical sampling of the noise in the spectra; specifically, we apply them in the generation of our synthetic spectra (see Section 3.3 for details). We make a further correction to these repeats by masking out any repeats that are $> 6\sigma$ from the mean of the repeats. This procedure and the reasoning behind it are also described in Section 3.3.

The caveat in using these repeats residuals is that, because these residuals are computed via a comparison between an individual exposure and a combined spectrum that is produced in part using this individual exposure (and thus contains information from it), the repeats residuals will be marginally smaller than the true error in the spectra. This is because the three residuals for a given star only have two degrees of freedom as a result of the combined spectrum containing information from the individual exposures to which it

is being compared. This means that we slightly underestimate the uncertainties in the spectra, thereby marginally overestimating the limits that we obtain on the intrinsic abundance scatter of the clusters; therefore, our constraints will be slightly more conservative than the true limits on the intrinsic abundance scatter of the clusters in this study (B16).

2.3.2 Masking and Other Uncertainty Corrections

In addition to our use of the repeats residuals on the simulated spectra that we produce, we perform several global corrections to the reported pixel-level uncertainties in the spectra, for both the observed and simulated spectra.

As mentioned above, the reported APOGEE uncertainties are significantly underestimated in large areas of the spectra. To specifically address this issue, we assume that uncertainties which result in a $\text{S/N} > 200$ are underestimated and adjust these underestimated uncertainties to have a S/N of 200.

Additionally, through the APOGEE_PIXMASK bitmask (Holtzman et al. 2015), APOGEE has identified several ‘bad’ pixels in each spectrum due to a variety of instrumental and observational effects. To account for these effects, we set the pixels in the observed and simulated spectra that have non-zero values in the APOGEE_PIXMASK bitmask to be NaNs, therefore removing them from consideration. A breakdown of the APOGEE_PIXMASK bitmask is given in Table 2.

After the bitmask corrections, we find that several pixels left unflagged in the bitmask still have very large errors, with $\text{S/N} \sim 0$. We remove these pixels from consideration as well, by setting pixels with $\text{S/N} < 50$ to be NaNs.

2.4 Red Clump Removal

In B16, red clump stars were removed from the analysis of C and N in M67 and all of the elements in NGC 6819, as the inclusion of these stars led to complications in the model. Similarly, we find that, for the open clusters that we test and for the birth clusters that we examine, members belonging to the red clump can affect our constraints on the abundance scatter of the clusters in a significant way. Red clump stars are low-mass, core He-burning stars, which have large convective envelopes (Girardi 2016), and their inclusion in our sample can lead to variations in the stellar spectra that are not captured by our model. For example, red clump stars display atypically low carbon isotope ratios due to deep mixing, changing the surface abundances of C and N (Gilroy & Brown 1991). When stars transition to the red clump after the He-flash, they therefore have a bimodal distribution in C and N as a function of T_{eff} that cannot be accounted for using our model (B16). Additionally, red clump stars have a lower $\log g$ than first-ascent red giant branch stars at the same T_{eff} in all elements (Girardi 2016), which leads to spectral fluctuations that also cannot be accounted for in our model.

We remove red clump stars from the open clusters that we test for consistency with B16, but in order to further avoid the issues discussed above, we remove all likely red clump members from our analysis of all of the elements in each of the open clusters that we test and the birth clusters that we analyze. We identify likely red clump members using the `rclsample` function in the APOGEE PYTHON package¹, which is part of the procedure to create the

¹ <https://github.com/jobovy/apogee>.

Table 1. Open and chemically-tagged birth clusters and the numbers of their members that we analyze. The ‘Number of Members’ column refers to the number of stars with temperatures between $4000 \text{ K} \leq T_{\text{eff}} \leq 5000 \text{ K}$ that are left in a particular cluster after uncertainty and error corrections (described in Section 2.3). The ‘Total Members Analyzed’ column refers to the number of stars on which we actually perform tests or analysis, after removing likely red clump stars identified by `rcsample`. The ‘Likely Red Clump Members’ column reports the number of stars identified by `rcsample` as red clump stars, which are removed from the analyzed sample of stars.

OCCAM open clusters (Donor et al. 2018)			
Cluster Name	Number of Members	Likely Red Clump Members	Total Members Analyzed
M67	22	3	19 (24 [*])
NGC 6819	19	7	12 (30 [*])
NGC 7789	16	8	16
NGC 6791	23	2	21

^{*} Analyzed in B16

Chemically-tagged birth clusters (Price-Jones et al. 2020)			
Cluster Name	Number of Members	Likely Red Clump Members	Total Members Analyzed
PJ 2	15	0	15
PJ 3	15	0	15
PJ 4	15	1	14
PJ 5	18	0	18
PJ 6	16	0	16
PJ 9	19	0	19
PJ 10	20	2	18
PJ 11	16	2	14
PJ 12	16	0	16
PJ 14	15	0	15
PJ 15	15	0	15
PJ 16	17	2	15
PJ 17	19	1	18
PJ 18	12	0	12
PJ 19	19	0	19
PJ 20	24	0	24
PJ 21	14	0	14

Table 2. APOGEE_PIXMASK bitmask flag descriptions used in the masks in this study (Holtzman et al. 2015).

Bit	Flag description
0	Pixel set as ‘bad’ according to the bad pixel mask
1	Pixel has a bad line-spread function
2	Pixel is saturated by a bright neighbour
3	Pixel is saturated by a very bright neighbour
4	Pixel has a bad dark frame
5	Pixel has a bad flat frame
6	Pixel error is very large
7	Pixel has no available sky from sky fibers
8	Pixel located in Littrow ghost
9	Pixel located in high persistence region
10	Pixel located in medium persistence region
11	Pixel located in low persistence region
12	Pixel is close to sky line
13	Pixel near telluric line
14	Good pixels contain fewer than half of star’s point-spread function

APOGEE red clump catalogue² (Bovy et al. 2014). This catalogue in DR14 is made up of 29, 502 likely red clump giant stars in APOGEE.

² https://www.sdss.org/dr14/data-access/value-added-catalogs/?vac_id=apogee-red-clump-rc-catalog.

To select these likely red clump stars, cuts on the APOGEE sample of stars were made using the following set of equations (Bovy et al. 2014; Abolfathi et al. 2018):

$$1.8 \leq \log g \leq 0.0018 \text{ dex K}^{-1} (T_{\text{eff}} - T_{\text{eff}}^{\text{ref}}([\text{Fe}/\text{H}]) + 2.4) \quad (3)$$

where

$$T_{\text{eff}}^{\text{ref}}([\text{Fe}/\text{H}]) = -382.5 \text{ K dex}^{-1} [\text{Fe}/\text{H}] + 4607 \text{ K}, \quad (4)$$

which correspond to Equations (2) and (3) in Bovy et al. (2014), respectively. Additional cuts were made on the $J_0 - K_{s,0}$ colours of these stars with respect to metallicity (Z) according to the equations

$$Z > 1.21[(J_0 - K_{s,0}) - 0.05]^9 + 0.0011 \quad (5)$$

$$Z < 2.58[(J_0 - K_{s,0}) - 0.40]^3 + 0.0034, \quad (6)$$

which correspond to Equations (6) and (7) in Bovy et al. (2014), with the additional bounds of

$$Z \leq 0.06, (J_0 - K_{s,0}) \geq 0.5, \quad (7)$$

which corresponds to Equation (8) in Bovy et al. (2014). A final cut on $\log g$ was made using the equation

$$\log g < 0.001 \text{ dex K}^{-1} (T_{\text{eff}} - 4800 \text{ K}) + 2.75, \quad (8)$$

which corresponds to Equation (9) in Bovy et al. (2014) (Abolfathi et al. 2018).

Absolute magnitude- T_{eff} diagrams are shown in Figure 1 for M67 and PJ 16. In each of these plots, the red clump stars are shown

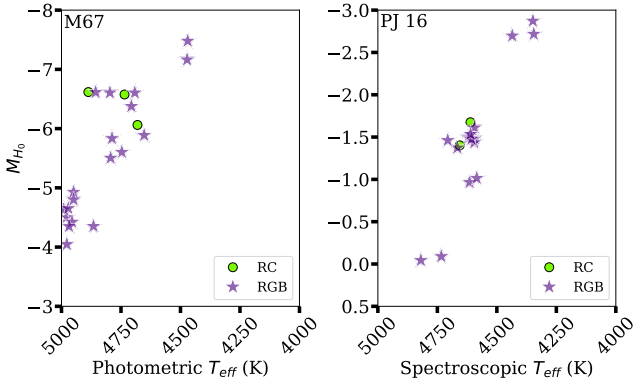


Figure 1. Examples of absolute H -band magnitude (M_{H_0}) vs. T_{eff} diagrams to illustrate some of the red clump stars within the open clusters that we use to test our method. Here, we show diagrams for the clusters M67 and PJ 16. The red clump stars (RC) are shown as green dots and the first-ascent red giant branch stars (RGB) are shown as purple stars. The distances used to compute the absolute magnitudes for M67 were obtained from OCCAM, where we use the distances that OCCAM records from Bailer-Jones et al. (2018). The distances used to compute the absolute magnitudes for PJ 16 were obtained from the ASTRONN VAC, which are a weighted combination of the distance estimated from Gaia parallax and the distance inferred by machine learning from APOGEE spectra and 2MASS photometry (Leung & Bovy 2019b).

as green dots and the first-ascent red giant branch stars are shown as purple stars. The number of likely red clump members for each cluster we analyze are reported in Table 1. For each cluster we study, we remove the likely red clump members identified in `rcsample` and use only the first-ascent red giant branch members.

Special note must be made of our treatment of the open cluster NGC 7789. After our cuts on T_{eff} and uncertainty corrections, NGC 7789 initially has the required number of 10 red giant members. However, after our cut on red clump stars, NGC 7789 is left with 8 first-ascent red giant branch members. We are still able to obtain tight constraints on the abundance scatter of this cluster, and so we complete our analysis of NGC 7789 with its 8 first-ascent red giant branch members.

3 METHODS

This section describes the way in which we model the APOGEE data and the method we use to constrain the level of chemical homogeneity in the chemically-tagged birth clusters. In this study, we make use of the APOGEE PYTHON package (see above). In order to infer tight constraints on the abundance scatter, we use a method that examines the effect of the abundance scatter on the spectra via forward modeling of the observed stellar spectra. In this way, we compare the abundance scatter in the chemically-tagged birth clusters directly to the spectral uncertainties. This method is robust to modeling errors that result from common stellar spectroscopy assumptions and to the major effects of stellar evolution on surface abundances (B16).

We model the spectra as a one-dimensional function of initial stellar mass, generate synthetic spectra that share the properties of the observed spectra, but with a variety of values of abundance scatter, and model them in the same way as the data. Finally, we compare the simulations and the data using Approximate Bayesian

Computation (ABC). This subsequently gives us an upper limit on the intrinsic abundance scatter in each open cluster modeled.

We will start by describing ABC from a general, theoretical standpoint (Section 3.1), followed by explaining how we model the data (Section 3.2), and how we generate synthetic spectra (Section 3.3). Finally, we will put all of these pieces together by describing how we use ABC in the context of this study (Section 3.6). We also test this method using the open clusters from OCCAM that are listed in Table 1 and the outcome of these tests will be discussed here. We use some individual chemically-tagged birth clusters as examples in the figures shown in this section, however we perform this same analysis on every cluster that we study.

3.1 Approximate Bayesian Computation

In Bayesian statistics, probability statements can be made for models, for the parameters of models, and for data. Here, inferences about probability are made by producing probability density functions (PDFs) and model parameters are treated as random variables. The Bayesian method makes use of all explicit and available information about a certain problem to produce optimal results (e.g., Ivezić et al. 2014).

Bayes' theorem quantitatively characterizes the Bayesian concept of combining prior knowledge with new data to develop an enhanced belief, given by the following expression:

$$p(M, \vec{\theta} | D, I) = \frac{p(D|M, \vec{\theta}, I)p(M, \vec{\theta}|I)}{p(D|I)} \quad (9)$$

where D represents the data and M represents the model. The model M is specified by k parameters θ_p , $p = 1, \dots, k$, represented as a vector $\vec{\theta}$ with components θ_p . More specifically, the components of Equation 9 are defined as: (a) $p(M, \vec{\theta} | D, I)$: the posterior PDF for M and $\vec{\theta}$, given D and other prior information I ; (b) $p(D|M, \vec{\theta}, I)$: the likelihood of the data, given M and $\vec{\theta}$, and all other prior information I ; (c) $p(M, \vec{\theta}|I)$: the prior, or the *a priori* joint probability for M and $\vec{\theta}$, without the data used to measure the likelihood $p(D|M, \vec{\theta}, I)$; and (d) $p(D|I)$: the prior predictive probability for D ; the probability of the data, which provides the proper normalization for the posterior PDF (e.g., Ivezić et al. 2014).

Approximate Bayesian Computation modifies Bayes' theorem in that it approximates the PDF without first evaluating the likelihood. Instead, forward simulations of the data (in this case, the synthetic spectra that we generate as described in Section 3.3) are used to approximate the likelihood (Sunnåker et al. 2013). Using ABC is advantageous when the likelihood of the data is difficult to compute; in the context of this study, computing the likelihood would involve a full, computable probability model for the residuals from the polynomial fit as a function of effective temperature that we perform for different values of intrinsic abundance scatter, which is difficult to generate (B16).

The steps involved in the ABC algorithm are as follows (Sunnåker et al. 2013):

- (i) A set of parameter points is sampled from a prior distribution.
- (ii) For a given sampled parameter point θ_p , a data set D' is simulated using the model M .
- (iii) If D' is significantly different from the observed data D according to a predefined threshold, the sample parameter value is rejected. One or several criterion $\rho(D', D)$ can be defined to represent the distance measure determining how different D and D' are, based on a given metric. In order for D' to be acceptably close

to D , $\rho(D', D) \leq \epsilon$, with $\epsilon \geq 0$ being the acceptability threshold for ‘sameness’.

As the dimensionality of a data set increases, the probability of being able to generate a simulated data set D' that is close to D decreases. To account for this, a set of lower-dimensional summary statistics $S(D)$ that encapsulate the information in D that is relevant can be used instead of D in the algorithm. In this case, the acceptance criterion for the ABC algorithm is defined as $\rho(S(D'), S(D)) \leq \epsilon$ (Sunnåker et al. 2013). It is important to note that there is inevitably some loss of constraining power in using these summary statistics, as they are not sufficient statistics which encode all information related to the inference at hand.

In summary, ABC is a useful technique that makes use of prior knowledge and new information to arrive at a conclusion about the probability of a certain result being possible. Its method of approximating the likelihood using forward simulations of the data is advantageous over the traditional Bayes’ theorem in cases where the likelihood of the data is difficult to compute.

3.2 The One-Dimensional Initial Stellar Mass Model

As alluded to previously, we model all spectra that we examine as a one-dimensional function of initial stellar mass. The framework that we use to model the spectra in our study is based on the fundamental assumption that there is no initial scatter in the birth abundances of a clusters’ member stars; therefore, the only significant difference between individual stars in a cluster is their initial masses. Moreover, we assume every differing photometric and spectroscopic property between individual stars can also be modeled as a one-dimensional function of their initial stellar masses. In the context of this study, this means that we model the stellar spectra near elemental absorption features as a one-dimensional function of initial stellar mass (B16).

However, initial stellar mass measurements are difficult to obtain, so we use the effective stellar surface temperatures (T_{eff}) of cluster members as a proxy for their initial stellar masses (B16). The way in which we use these T_{eff} differs for the OCCAM open clusters and the blindly chemically-tagged open clusters.

For our test of the method using the OCCAM clusters, we use photometric T_{eff} , calculated using the expression

$$T_{\text{eff}} = \frac{5040 \text{ K}}{b_0 + b_1 X + b_2 X^2 + b_3 X[\text{Fe}/\text{H}] + b_4 [\text{Fe}/\text{H}] + b_5 [\text{Fe}/\text{H}]^2} \quad (10)$$

which corresponds to Equation (10) in González Hernández & Bonifacio (2009), where X represents the colour (in this case $J_0 - K_{s,0}$, which are obtained from APOGEE and de-reddened) and b_i ($i = 0, \dots, 5$) are the coefficients of the fit given in Table 5 in González Hernández & Bonifacio (2009). Photometric T_{eff} were also used in B16. Crucial to our use of Equation (10) is the use of de-reddened colours. We take J and K_s colours from 2MASS (Skrutskie et al. 2006) and in correcting those colours for extinction we use the median values of A_{K_s} as given in the APOGEE catalogue, because the distributions of these quantities measured in APOGEE are not as uniform as we would expect (each star in a particular open cluster should have approximately the same amount of extinction due to all of the stars’ similar distances away from Earth). We assume that this is due to random errors in the extinctions and take the median value of A_{K_s} to best represent the true value for the entire cluster. For consistency, we also use the median value of $[\text{Fe}/\text{H}]$ in computing the photometric T_{eff} using Equation (10). In the

case of the OCCAM clusters, we use these photometric T_{eff} instead of APOGEE’s spectroscopic T_{eff} because they are independent of the spectra that we use to test our method.

For the chemically-tagged birth clusters, we use the reported APOGEE spectroscopic T_{eff} . We do not use the photometric T_{eff} in this case because we do not have as good of an understanding of the extinction values for these clusters’ member stars, as the members of each cluster are scattered across the Galactic disc.

To model the spectra as a one-dimensional function, we perform a simple quadratic fit to the data. For each pixel corresponding to the non-zero weights of each element (described in Section 2.1.1), we compute a quadratic fit of the spectral flux versus T_{eff} (either photometric or spectroscopic). These fits are done for each cluster that we analyze and for each element individually. Specifically, this means that we model the flux at each pixel (where each pixel corresponds to a different wavelength) for each non-zero elemental spectral weight in each star as a function g_{λ} , characterized by the fitting parameters θ_{λ} plus the measurement noise, according to the expression

$$f_{\lambda}^i = g_{\lambda}(T_{\text{eff},i} | \theta_{\lambda}) + \text{noise} \quad (11)$$

where f is the flux of a star and the index i labels the individual stars. To perform these fits, we apply a least squares fitting routine that accounts for the known Gaussian uncertainties in the data, using the procedure described in Hogg et al. (2010). We compute the fit residuals r_{λ}^i using the following expression:

$$r_{\lambda}^i = f_{\lambda}^i - g_{\lambda}(T_{\text{eff},i} | \theta_{\lambda}). \quad (12)$$

and normalize these fit residuals by dividing out the pixel-level uncertainties, corrected as described in Section 2.3.

We then compute cumulative distributions of the normalized fit residuals using the pixel weights for each element in each cluster individually, as well as for the combined spectra of all cluster members. Plots displaying example cumulative distributions of the normalized fit residuals for the birth cluster PJ 6 are shown in Figure 2 and described in Section 3.5. The cumulative distributions of the normalized fit residuals of all of the birth clusters that we analyze in this study are compared in Figure 7 and described in Section 4. A similar comparison for the OCCAM open clusters is shown in Figure 5 in Section 3.7.

In summary, we model all spectra that we consider as a one-dimensional function of initial stellar mass, using effective surface temperature as a proxy for initial stellar mass, and perform quadratic fits of the temperature dependence of the flux in each pixel. We take the normalized residuals from these fits and use them to produce cumulative distributions. This model is useful because it allows us to model all spectroscopic and photometric effects that differ between cluster members, which could in principle affect the surface abundances of these stars (e.g., internal mixing), as a one-dimensional function of initial stellar mass and constrain their importance, reducing the complexity of the problem that we are trying to study significantly.

3.3 Generating Synthetic Spectra

To fulfill the forward modeling component (to produce the D') of the ABC algorithm described in Section 3.1, we produce several synthetic APOGEE spectra for each open cluster by applying the POLYNOMIAL SPECTRAL MODELING (PSM) code by Rix et al. (2016) to the parameters of each star in each cluster. To produce a set of mock synthetic spectra, we draw a random value of intrinsic abundance scatter $\sigma_{[\text{X}/\text{H}]}$ from a uniform prior of 0 to 0.1 dex, which

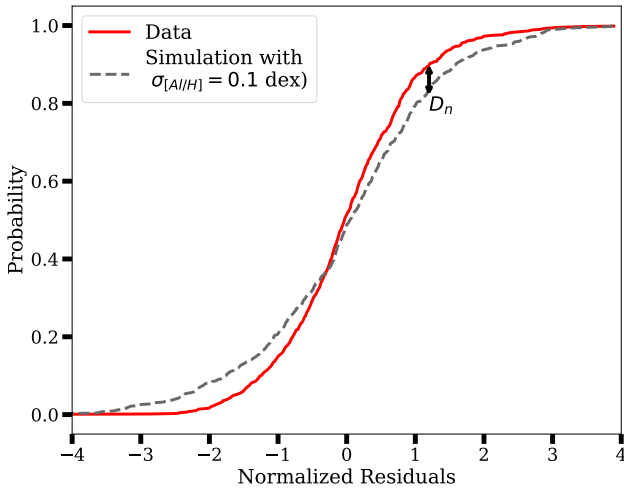


Figure 2. Examples of cumulative distributions of normalized fit residuals for Al in cluster PJ 6. The cumulative distribution of the normalized residuals for Al obtained from fitting the observed spectra is represented by the red curve. The cumulative distribution of the normalized residuals obtained from fitting a set of simulated spectra with a simulated abundance scatter of $\sigma_{[Al/H]} = 0.1$ dex is represented by the dashed grey curve. A visual representation of how the summary statistic D_n is computed is shown via the black arrow; D_n is the maximum absolute difference between the cumulative distribution of the normalized residuals from the observed spectra and that of a set of simulated spectra.

represents the sampled parameter point θ_P used to simulate D' from our discussion of the ABC algorithm. We draw synthetic elemental abundances from a normal distribution centred at the average $[X/H]$ abundances of the cluster for each element X, with a standard deviation of the chosen value of $\sigma_{[X/H]}$. We vary one element per simulation and keep the remaining elements at their observed chemical abundances. We feed these simulated abundances into the PSM code along with the observed T_{eff} (where we use photometric T_{eff} for the OCCAM clusters and spectroscopic T_{eff} for the PJ clusters, as discussed in Section 3.2), $\log g$ from APOGEE, and the PSM default values of v_{turb} and C_{12}/C_{13} for each cluster.

Spectra in DR14 and later data releases extend over a slightly wider wavelength range than those in DR12. To account for the fact that the PSM code was written for APOGEE DR12, we only consider parts of the observed spectra that lie within the DR12 spectral ranges. The drawback from this procedure is that some chemical information captured by elemental absorption features located at the edges of the detectors is lost. However, overall, very few absorption lines are cut out of our analysis as a result of this procedure, leaving us with enough chemical information to perform the analysis on each APOGEE element.

In keeping with producing synthetic spectra that are very similar to the observed spectra, we also use the APOGEE_PIXMASK bitmask (Holtzman et al. 2015) to mask the same bad pixels in the synthetic spectra as in the observed spectra.

To make our simulated spectra more realistic, we create synthetic noise by drawing a random set of repeats residuals from those created using the procedure described in Section 2.3 for each star in the observed stellar spectra and multiply these repeats by the observed spectral errors. As discussed in Section 2.3, we multiply the repeats by the observed spectral errors to produce more realistic noise for our synthetic spectra, because the reported APOGEE un-

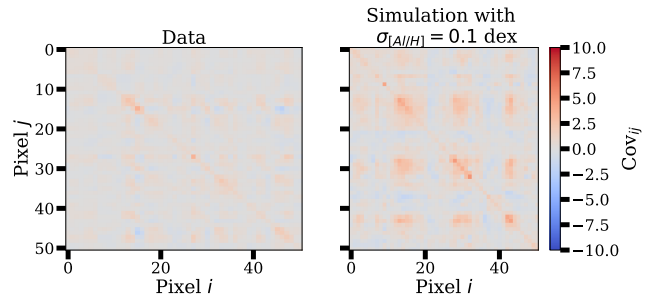


Figure 3. Examples of covariance matrices of normalized residuals for Al in PJ 6. The covariance matrix of the normalized residuals obtained from fitting the observed spectra is shown in the left panel. The covariance matrix of the normalized residuals obtained from fitting a set of simulated spectra with a simulated abundance scatter of $\sigma_{[Al/H]} = 0.1$ dex is shown in the right panel. Each pixel in the windows for Al are shown on the x- and y-axes and the colour bar represents the amount of covariance between each pixel. To compute the covariance matrix summary statistic, the values of the covariance between each pixel in the observed spectra are subtracted from the values of the covariance between each corresponding pixel in the simulated spectra, and then manipulated as per Equation 14.

certainties were found to be underestimated. We add the quantities that we obtain from multiplying the repeats by the observed spectral errors to the simulated spectra to create synthetic noise.

Because the repeats residuals do not necessarily consist of the same stars as the ones we are analyzing, they are consequently masked by the APOGEE_PIXMASK bitmask in different areas, which results in the synthetic spectra being masked in additional places in comparison to the observed spectra. To account for this, we mask the observed spectra in these places as well. Additionally, we notice that there are some individual repeats with absolute values that are unrealistically large, and as such affect our results for constraints on the intrinsic abundance scatter for our clusters. We assume this is due to a systematic error and avoid these repeats by masking out any pixels in both the simulated and observed spectra that correspond to the individual randomly selected repeats that are $> 6\sigma$ from the mean of the repeats.

After we produce these spectra using all of the above considerations, we model the synthetic spectra in the same way as the observed stellar spectra, using the one-dimensional initial stellar mass model described in Section 3.2.

In summary, we produce synthetic spectra for each cluster using the PSM code from Rix et al. (2016) by drawing a random value of intrinsic abundance scatter and using this value to simulate the chemical abundances of the cluster in question. We make these synthetic spectra look as similar to the observed spectra as possible by applying a variety of masking procedures and by producing synthetic noise that we add to the simulated spectra.

3.4 Summary of Uncertainty Corrections

Once we generate the synthetic spectra, we apply the corrections described in Section 2.3 to both the observed and simulated spectra. The order in which we apply the corrections are outlined here:

- (i) For the observed and simulated spectra:
 - (a) Adjust underestimated uncertainties with $S/N > 200$ to have $S/N = 200$.

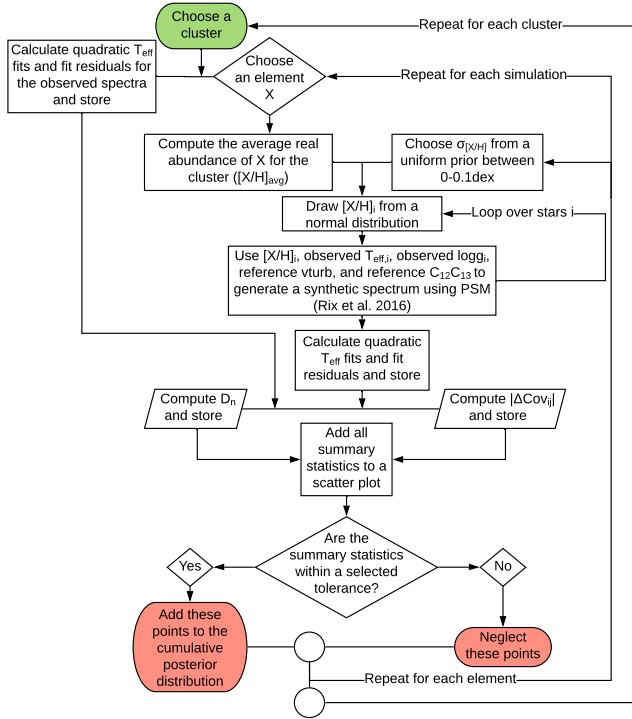


Figure 4. The steps involved in the ABC algorithm. We repeat the algorithm until a large enough number of simulations that produce appropriate $|\Delta \text{Cov}_{ij}|$ and D_n for a given threshold are obtained.

- (b) Apply the APOGEE_PIXMASK bitmask (these bits will be set to NaNs and neglected).
- (c) Mask large-error pixels with $S/N < 50$ (these points will be set to NaNs and neglected).
- (d) Mask pixels outside of the bounds of the DR12 detectors (described in Section 3.3).
- (ii) For the simulated spectra:
 - (a) Produce mock noise to add to the spectra by drawing from the repeats residuals, which will further mask the spectra (described in Section 3.3).
 - (b) Mask values of the chosen repeats that are $> 6\sigma$ away from the mean.
- (iii) For the observed spectra:
 - (a) Re-mask the observed spectra to match the new masking in the simulated spectra that results from the application of the repeats residuals (described in Section 3.3).

Once all of these corrections are completed, we fit the data as in Section 3.2, fitting only those pixels that have ≥ 5 stars remaining after all uncertainty and error considerations have been applied. If an element has less than 5 stars remaining after the uncertainty and error considerations are applied for every pixel, we neglect that element in our analysis.

3.5 Summary Statistics

As discussed in Section 3.1, summary statistics $S(D)$ that capture the relevant information in the data set D can be used instead of D in the ABC algorithm when the dimensionality of D is high (Sunnåker

Table 3. The 95% upper limits on the constrained intrinsic abundance scatter for the 15 APOGEE elements for the open clusters in OCCAM that we analyze. A dashed entry indicates that not enough data is available for the element in question after we complete the masking and uncertainty corrections.

	M67	NGC 6819	NGC 7789	NGC 6791
C	0.038	0.061	0.047	0.07
N	0.055	0.041	0.067	0.084
O	0.054	0.095	0.063	0.092
Na	0.094	-	-	-
Mg	0.035	0.046	0.067	0.096
Al	0.04	0.097	0.09	0.098
Si	0.031	0.051	0.062	0.094
S	0.077	0.097	0.095	0.096
K	0.083	0.083	0.092	0.094
Ca	0.036	0.058	0.066	0.098
Ti	0.091	0.097	0.097	0.097
V	0.092	0.098	0.094	0.098
Mn	0.031	0.061	0.068	0.092
Fe	0.021	0.035	0.043	0.089
Ni	0.038	0.051	0.071	0.096

et al. 2013). Here, we make use of two summary statistics computed using the residuals from the one-dimensional fit to each wavelength pixel: the Kolmogorov-Smirnov distance and a statistic describing the difference between the covariance matrices of the normalized residuals of different pixels for the observed and simulated data (B16).

The Kolmogorov-Smirnov distance (D_n) is defined as the maximum absolute difference between the cumulative distributions of the normalized residuals of the data and the normalized residuals of a simulation, as computed in Section 3.2. Explicitly, if the cumulative distribution of the normalized residuals of the data is defined by a function $F_0(x)$ and the cumulative distribution of the normalized residuals of a simulation is defined by a function $S_N(x)$, then the Kolmogorov-Smirnov distance between the data and the simulation is given by the following expression (Massey Jr. 1951):

$$D_n = \text{maximum}|F_0(x) - S_N(x)| \quad (13)$$

A visualization of how we compute D_n is shown in Figure 2.

To determine the covariance matrix summary statistic, we compute the covariance matrix Cov_{ij} of the residuals between pixels i and j for the data and a simulation. We then compute the difference between the covariance matrices for the data and the simulation for each simulation, according to the following expression:

$$|\Delta \text{Cov}_{ij}| = \sqrt{\sum_{ij} (w_i w_j)^{1/2} (\text{Cov}_{ij}^{\text{data}} - \text{Cov}_{ij}^{\text{sim. data}})^2} \quad (14)$$

where w_i and w_j are the pixel-level weights for a given element (see Section 2.1.1). Examples of covariance matrices of the normalized fit residuals for the data and a simulation with an abundance scatter of $\sigma_{[\text{Al}/\text{H}]} = 0.1$ dex are shown for Al in PJ 6 in Figure 3, as a visual representation of the covariance matrix summary statistic.

Each of these summary statistics is important in characterizing the upper limit on the abundance scatter in the clusters that we analyze. $|\Delta \text{Cov}_{ij}|$ gives strong constraints on the scatter $\sigma_{[\text{X}/\text{H}]}$, since it is strongly correlated with $\sigma_{[\text{X}/\text{H}]}$. D_n gives information about the shape of the distribution of the residuals (B16).

3.6 The ABC Algorithm in the Context of this Study

To quantitatively determine the constraints on the intrinsic abundance scatter in the chemically-tagged birth clusters that we analyze, we use the ABC algorithm to construct an approximation of the posterior PDF of the scatter in each element. The specific steps that we use in the context of this study are described in the flow chart in Figure 4.

For a given element X, we begin by drawing a value of abundance scatter $\sigma_{[X/H]}$ for each element X from a uniform prior of between 0 and 0.1 dex, and then generate synthetic spectra as described in Section 3.3. We fit the T_{eff} dependence of each pixel using the one-dimensional quadratic model described in Section 3.2. We also mask the observed spectra in the same way as the synthetic spectra, and then fit the T_{eff} dependence of each pixel using the one-dimensional quadratic model as well.

We compute cumulative distributions of the normalized fit residuals for each of the data and the simulations using the spectral weights for an element X and compare these via the Kolmogorov-Smirnov distance (D_n), as defined in Equation (13), described in Section 3.5, and illustrated visually in Figure 2. We also compute covariance matrices of the normalized fit residuals for each of the data and the simulations and compare these via the covariance matrix statistic as defined in Equation (14), described in Section 3.5, and illustrated visually in Figure 3.

For each set of simulations for an element X, we plot the values of D_n and $|\Delta\text{Cov}_{ij}|$ on a scatter plot. Examples of these plots are shown in Figure 8 and are described in Section 4. To determine the upper limits on the intrinsic abundance scatter in the clusters we examine, we select simulations that ‘match’ the data in that they have small values of both $|\Delta\text{Cov}_{ij}|$ and D_n , as in Figure 8. In this way, we focus the study on the limiting of the abundance scatter rather than deviations between the simulations and the data (B16). We then create cumulative posterior distribution functions of the values of $\sigma_{[X/H]}$ that correspond to these simulations that match the data, examples of which are shown in Figure 6 and described in Section 3.7 for the OCCAM open clusters and in Figure 9 and described in Section 4 for the PJ birth clusters, for the elements Al, V, and Fe as examples. From these cumulative posterior distribution functions, we determine the upper limits on the intrinsic abundance scatter for each element at a confidence level of 95%. This allows us to identify the value of the abundance spread that produces the simulated spectra that are closest to the observed spectra, thus constraining the abundance spread.

We run simulations until these limits and the distributions of D_n and $|\Delta\text{Cov}_{ij}|$ appear to have converged by eye ($\sim 10,000$ simulations in total and we use $\sim 700 - 1,000$ simulations that are very close to the data to determine the upper limits on the intrinsic abundance scatter). Once we have achieved convergence, we report the final upper limits on the intrinsic abundance scatter at a confidence level of 95%, as shown in Table 3 in Section 3.7 for our test on the OCCAM open clusters and in Table 4 in Section 4 for our analysis of the chemically-tagged birth clusters below.

3.7 Testing the Method with Open Clusters

To test our implementation of the method described here, we run the algorithm on the four open clusters that we study from OCCAM. We perform the one-dimensional initial stellar mass fitting procedure described in Section 3.2 on the observed spectra, where we see that the distribution of the residuals is consistent with the uncertainty distribution for each pixel of the observed spectra, similar to the

results in B16, indicating that this one-dimensional model provides a good fit.

We perform the same fitting procedure on the simulated data sets. For simulations with $\sigma \rightarrow 0.1$ dex, the residuals are much larger than the reported uncertainties, as in B16, implying that the scatter around the quadratic fit is strongly constraining for the intrinsic abundance scatter.

After we complete the fits, we normalize the fit residuals by dividing out the corrected pixel-level uncertainties and then compute cumulative distributions of the normalized fit residuals, as described in Section 3.2. A comparison of the cumulative distributions for each open cluster from OCCAM to the cumulative distribution of the noise (represented by the dotted grey curve) and the cumulative distribution of the normalized residuals from a simulation of M67 with $\sigma_{[X/H]} = 0.1$ dex (represented by the dashed black curve) are shown in Figure 5. From this figure, it is clear that the simulation has a much wider distribution than that of the observed spectra. The cumulative distribution of the data is steeper and centred at zero, indicating that the fit residuals lie at or near zero and that the quadratic T_{eff} model fits the data well.

To quantitatively determine the constraints on the abundance scatter in the open clusters that we analyze, we apply the algorithm described in Section 3.6. Examples of summary statistic scatter plots are shown in Figure 8 for some of the PJ clusters, which will be described in Section 4, and we make similar visualizations in the analysis of the OCCAM open clusters here.

We compute cumulative posterior distribution functions from simulations of each cluster in every element, using the simulations with values of $\sigma_{[X/H]}$ that are close to the data (captured by threshold boxes similar to those in Figure 8 for the PJ clusters, as an example). These cumulative posterior distributions are shown in Figure 6 for Al, V, and Fe in each cluster in OCCAM, as examples. Those for M67 are represented by the solid red curves, those for NGC 6819 are represented by the tightly dot-dashed yellow curves, those for NGC 7789 are represented by the loosely dot-dashed blue curves, and those for NGC 6791 are represented by the dot-dot-dashed green curves.

The upper limits on the intrinsic abundance scatter at 95% confidence for each element are reported in Table 3 for each cluster in OCCAM that we use to test our method. We obtain strong constraints ($\lesssim 0.05$ dex at 95% confidence) on several elements in each individual cluster (i.e. C, Mg, Al, Si, Ca, Mn, Fe, and Ni in M67, N, Mg, and Fe in NGC 6819, and C and Fe in NGC 7789), but the limits on the majority of the elements in the open clusters that we test are weak. Specifically, we obtain weak limits on all of the elements in NGC 6791. However, given that NGC 6791 is very metal-rich (Donor et al. 2018), it is not surprising that we are unable to obtain strong limits for this cluster in particular.

In comparing the results of our test to those from B16 for M67 and NGC 6819, there are some minor differences in the upper limits on the intrinsic abundance scatter of these open clusters. The weaker constraints that we obtain for elements such as Na, S, K, Ti, and V are not necessarily surprising, since these elements have very few pixels over which we are able to do our analysis compared to the remaining elements in APOGEE, due to our choice of mask described in Section 2.3, which is more aggressive than that used in B16. Additionally, the abundances for Na, Ti, and V have been cited as being unreliable in APOGEE (Ting et al. 2015).

The differences in the upper limits on the remaining elements are easily explained by the major differences in the method used between this study and that in B16. For example, as described in Section 2.1.1, there are significant differences between the DR12

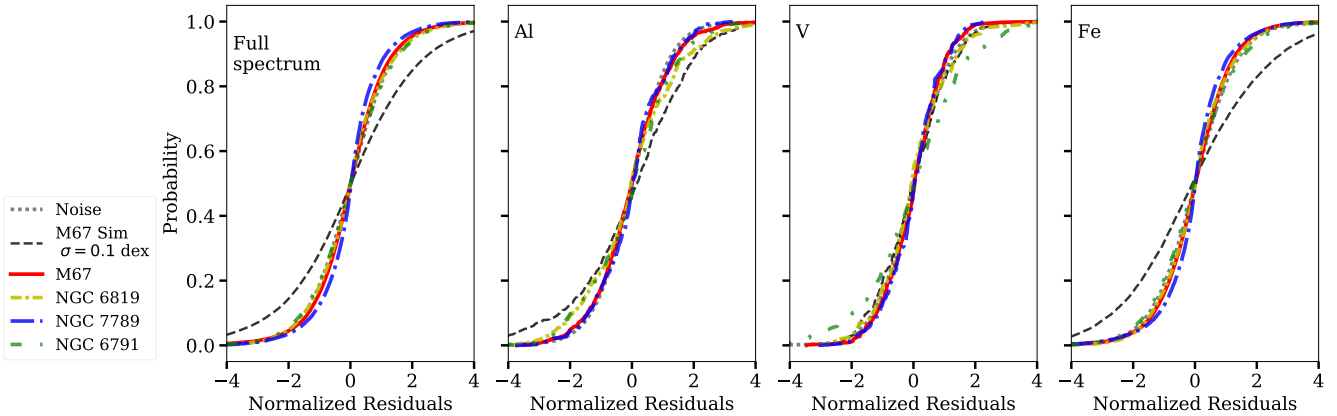


Figure 5. The cumulative distributions of the normalized residuals from the quadratic T_{eff} fits for the OCCAM open clusters. The cumulative distribution of all pixels in the spectra is shown in the left-most panel for each open cluster in OCCAM and the subsequent panels display the cumulative distributions for the fit residuals weighted by the pixel weights that emphasize the pixels most affected by Al, V, and Fe, for example (see Section 2.1.1). In each panel, M67 is represented by the solid red curve, NGC 6819 is represented by the tightly dot-dashed yellow curve, NGC 7789 is represented by the loosely dot-dashed blue curve, and NGC 6791 is represented by the dotted grey curve, corresponding to the noise in the spectra. Additionally, the cumulative distributions of the normalized residuals for a simulation of M67 with $\sigma_{[X/H]} = 0.1$ dex for each element X is represented by the dashed black curve; this level of intrinsic abundance scatter would produce much larger residuals than observed.

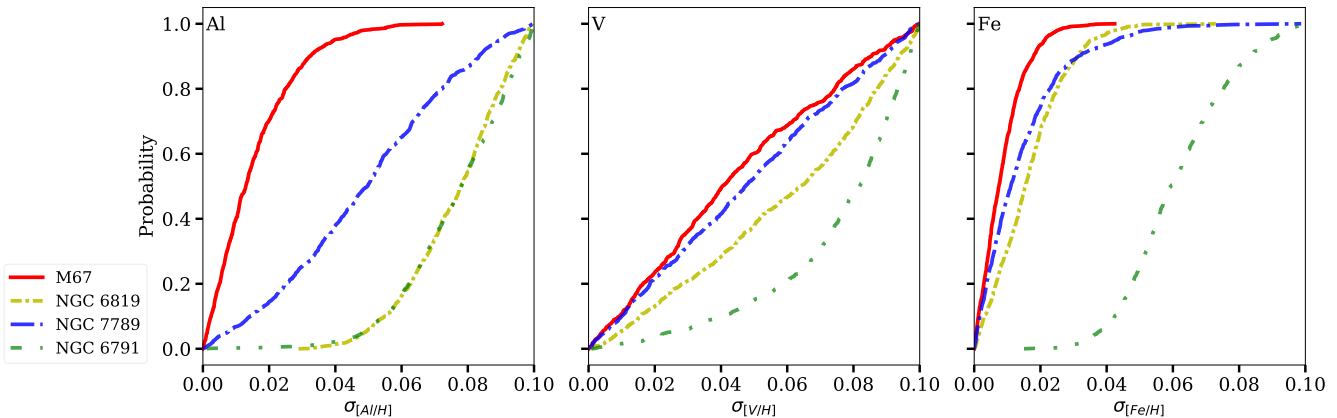


Figure 6. The cumulative posterior distribution functions for the intrinsic abundance scatter in Al, V, and Fe as examples, in each open cluster from OCCAM that we study. Here M67 is represented by the solid red curve, NGC 6819 is represented by the tightly dot-dashed yellow curve, NGC 7789 is represented by the loosely dot-dashed blue curve, and NGC 6791 is represented by the dot-dot-dashed green curve. The 95% upper limits for each OCCAM cluster are reported in Table 3.

windows and the DR14 windows. Specifically for elements like C and N, in which the number of windows increased significantly between DR12 and DR14, the increased number of windows could be resulting in increased contamination from other elements. While the windows are weighted to give the most significance to the element in question and less significance to other elements, there are still pixels that overlap between elements, and a certain amount of signal could be contributed by elements other than the one that is specifically being considered.

We also perform more aggressive masking and uncertainty-correction procedures which may lead to weaker overall constraints on the intrinsic abundance scatter of open clusters. As a result of this and our red clump star removal, we use fewer stars in our analysis of M67 and NGC 6819 than B16. It is also important to note that

not all of the clusters in our study that were also analyzed in B16 (i.e. M67 and NGC 6819) are able to be studied in the same way. Because of variations between the catalogue from Mészáros et al. (2013) used to identify open cluster members in B16 and our use of OCCAM (Donor et al. 2018), the member red giant stars are not all consistent between the two studies (i.e. of the 19 members we analyze in M67, 10 of them are also analyzed in B16 and of the 12 members we analyze in NGC 6819, 7 of them are also analyzed in B16).

An additional difference between this study and that completed in B16 is the way in which we generate our synthetic spectra. Specifically, we use the PSM code, while B16 uses TURBOSPECTRUM. TURBOSPECTRUM produces synthetic spectra by directly solving the radiative transfer equation using input data such as opacities (Al-

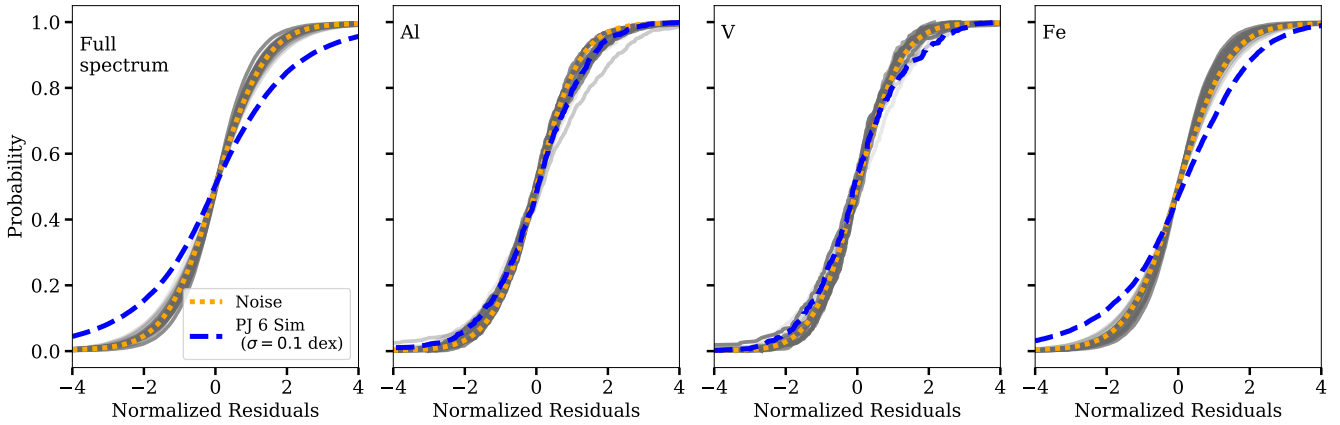


Figure 7. The cumulative distributions of the normalized residuals from the quadratic T_{eff} fits for the PJ birth clusters. The cumulative distribution of all pixels in the spectra is shown in the left-most panel and the subsequent panels display the cumulative distributions of the normalized fit residuals weighted by the pixel weights that emphasize the pixels most affected by Al, V, and Fe, respectively (see Section 2.1.1). In each panel, the cumulative distributions of each of the PJ birth clusters are represented by the series of grey curves. The cumulative distributions of the repeats residuals (as discussed in Section 2.3.1) are represented by the dotted orange curve, corresponding to the noise in the spectra. Additionally, the cumulative distributions of the normalized residuals for a simulation of PJ 6 with $\sigma_{[X/H]} = 0.1$ dex for each element X is represented by the dashed blue curve. Overall, the fit residuals for the PJ clusters are consistent with the noise, thus requiring little to no intrinsic abundance scatter.

varez & Plez 1998), while PSM constructs a polynomial spectral model of order O for the model flux at each wavelength to approximate the spectra (Rix et al. 2016) based on a small set of synthetic spectra computed with a code similar to TURBOSPECTRUM.

Taking all of these differences between the methods into account, we are able to achieve relatively similar constraints on the abundance scatters in the open clusters M67 and NGC 6819 when compared to B16, excluding those elements that have very few pixels over which we can do our analysis (i.e. Na, S, K, Ti, and V). Thus, we have calibrated our method via this test using the open clusters, and can therefore use it to analyze the chemically-tagged birth clusters from Price-Jones et al. (2020).

4 RESULTS

In this section, we present the results of our analysis of the blindly chemically-tagged birth clusters identified by Price-Jones et al. (2020). We perform the ABC algorithm as described in Section 3 on these birth clusters; that is, we complete the one-dimensional initial stellar mass fitting procedure as described in Section 3.2 and compute the cumulative distributions of the normalized residuals. Figure 7 shows a representation of all of the cumulative distributions from all of the analyzed PJ clusters, represented by the series of grey curves, compared to a cumulative distribution of the noise (computed from the repeats residuals, described in Section 2.3.1), represented by the dotted orange curve, and a cumulative distribution of the normalized fit residuals from a simulation of PJ 6 with an abundance scatter of $\sigma_{[X/H]} = 0.1$ dex, represented by the dashed blue curve. The cumulative distribution of all of the pixels in the spectrum is shown in the left-most panel and the subsequent panels display the cumulative distributions of the fit residuals for Al, V, and Fe. Similar to Figure 5, it is clear that the simulation has a much wider distribution than that of the observed spectra. The cumulative distributions of the data from most of the PJ clusters are steeper and centred at zero, indicating that the fit residuals lie at or near zero and that the quadratic T_{eff} model fits the data well.

We then apply the ABC algorithm described in Section 3.6 and plot the distributions of the summary statistics obtained for each set of simulations on scatter plots. Example scatter plots are shown in Figure 8, where the D_n summary statistic is shown on the x-axis and the $|\Delta\text{Cov}_{ij}|$ is shown on the y-axis. The colour bar represents the different values of $\sigma_{[X/H]}$ that we draw for each simulation. The left panel displays the summary statistics for simulations with intrinsic scatter in Al in PJ 6, the middle panel displays those with intrinsic scatter in Fe in PJ 20, and the right panel displays those with intrinsic scatter in Si in PJ 5. We show these particular elements in these specific clusters as examples, but we create visualizations like these for every element in every birth cluster that we study.

The panels for Al in PJ 6 and Fe in PJ 20 in Figure 8 represent ideal summary statistic behaviour. It is important to note that, while most of the elements that have enough pixels for analysis in most of the birth clusters that we study display this behaviour, not all of the elements in all of the clusters that we analyze are as well-behaved. Specifically, some elements show a ‘turning-back’ behaviour, which indicates potential intrinsic abundance scatter. This behaviour is exemplified by the panel for Si in PJ 5 in Figure 8, where it is clear that the tail of simulations with $\sigma_{[X/H]} \rightarrow 0$ turns back toward increasing D_n , as opposed to being focused at small D_n and $|\Delta\text{Cov}_{ij}|$ as in the panels for Al in PJ 6 and Fe in PJ 20. Specifically, this plot seems to indicate that there is intrinsic abundance scatter in Si in PJ 5. This kind of behaviour is also seen in Mg and Al in PJ 4, all of the elements in PJ 5, C, Al, Si, and Ni in PJ 9, Al and Si in PJ 10, Mn in PJ 12, O and Fe in PJ 14, Mg in PJ 15, Ti and Mn in PJ 16, every element except for C, N, and Ni in PJ 17, O, Si, Ca, V, and Mn in PJ 18, O, Mg, Si, Ca, Ti, Mn, and Ni in PJ 19, and every element except for C, N, and Fe in PJ 21. However, the behaviour of the majority of the summary statistic plots of the PJ clusters is generally indicative of chemical homogeneity.

We compute cumulative posterior distribution functions for each element and each cluster using the values of $\sigma_{[X/H]}$ captured by the threshold boxes in the summary statistic plots for each element, examples of which are shown in Figure 8. Since we find little evidence overall for abundance scatter in all of the elements in most

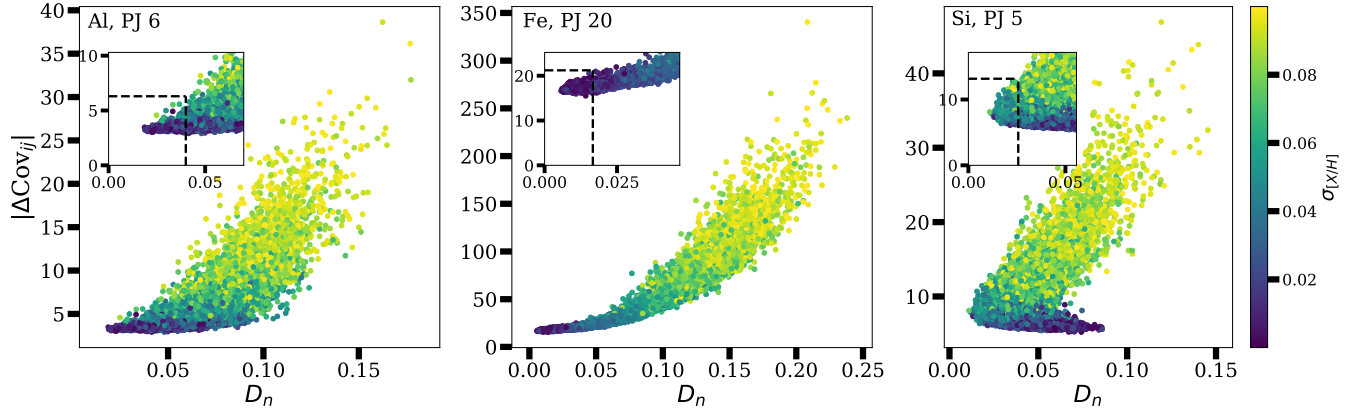


Figure 8. A visualization of the two summary statistics we compute in the ABC algorithm to compare the observed spectra to the simulated spectra, for a sample of the chemically-tagged birth clusters that we study. The left panel displays the simulations with intrinsic scatter in Al in PJ 6, the middle panel displays the simulations with intrinsic scatter in Fe in PJ 20, and the right panel displays the simulations with intrinsic scatter in Si in PJ 5. The Kolmogorov-Smirnov distance (D_n) is shown on the x -axis and the covariance matrix statistic ($|\Delta\text{Cov}_{ij}|$) is shown on the y -axis. To compute these summary statistics, we use the residuals weighted for each respective element in each panel. The colour bars represent the different values of $\sigma_{[X/H]}$ that we use for each simulation, where X is Al, Fe, or Si in these examples. The inset panels display the simulations that are closest to the data (i.e. where both summary statistics are small) and the dashed lines within show the thresholds we use to define the constrained $\sigma_{[X/H]}$.

of these birth clusters (excluding those elements that have very few pixels), we can combine the cumulative posterior distribution functions to obtain a combined constraint on the intrinsic abundance scatter. Specifically, in this calculation, we assume that all of the clusters have the same intrinsic abundance scatter and we place a limit on this (B16). A summary of the cumulative posterior distribution functions for Al, V, and Fe in APOGEE is shown in Figure 9. We show these summary curves as opposed to the individual cumulative posterior distribution functions as in Figure 6 for OCCAM for ease of visualization. The black curve in each panel represents the cumulative posterior distribution of all of the combined PJ birth clusters. The four additional curves in each panel represent the cumulative posterior distribution functions for the clusters that have the maximum and minimum upper limits in each element, as well as those that have upper limits that are approximately 33% and 66% of the way between the minimum and maximum upper limits. The curve for the cluster with the minimum upper limit on the intrinsic abundance scatter is the steepest curve in each panel and the curve for the cluster with the maximum upper limit on the intrinsic abundance scatter is the shallowest curve in each cluster.

From these cumulative posterior distribution functions, we can quantify the upper limits on the intrinsic abundance scatter of each birth cluster. Table 4 describes the upper limits on the intrinsic abundance scatter at 95% confidence for each of the 15 APOGEE elements for the blindly chemically-tagged birth clusters we analyze.

Overall, we obtain much stronger limits on the intrinsic abundance scatter in the PJ clusters than the OCCAM clusters, with the combined constraints generally being strong. Specifically, we obtain strong constraints ($\lesssim 0.05$ dex at 95% confidence) on every element except for Na, Al, S, K, Ti, and V.

Figure 10 provides a visual summary of the constraints that we obtain for each element in the PJ clusters. Here, the median constraint on each element across all of the birth clusters is represented by the black arrows. The maximum constraint on each element is represented by the orange arrows, and the minimum constraint on each element is represented by the red arrows. The interquartile range of the constraints on each element across all of the birth clusters is represented by the grey regions.

ters is represented by the blue region. The arrows for each respective statistic have been connected by lines for ease of visualization (i.e. solid black lines for the median, dotted orange lines for the maximum, and dashed red lines for the minimum). Additionally, the elements that were used by Price-Jones et al. (2020) to associate the birth clusters are highlighted using vertical grey lines (i.e. Mg, Al, Si, K, Ti, Mn, Fe, and Ni).

Figure 11 provides another visual summary of the our constraints on the PJ clusters, but this time across the clusters as opposed to across the elements as in Figure 10 above. We have separated these results into four groups, where the constraints on some of the α -elements for each PJ cluster are shown in the top left panel, the constraints on the Fe-peak elements are shown in the top right panel, the constraints for some of the odd-Z elements are shown in the bottom left panel, and the constraints for C and N are shown in the bottom right panel. We exclude some of those elements with few pixels available for analysis from this visualization (i.e. Na, S, Ti, and V), as their constraints are generally weak and not representative of the entire sample. In each panel, the medians of the constraints for the elements shown in each panel are represented by the black arrows, which are connected by the solid black lines for ease of analysis. The interquartile ranges of the constraints for the elements shown in each panel are represented by the grey regions in each panel.

5 DISCUSSION

5.1 Elemental Variation in Abundance Scatter Constraints

As can be seen from comparing the summary statistic plots for Al in PJ 6 and Fe in PJ 20 to Si in PJ 5 in Figure 8, there are two main types of behaviour that appear in the summary statistics for elements with an appropriate number of pixels available for analysis: that of chemical homogeneity (i.e. Al in PJ 6 and Fe in PJ 20) and that of intrinsic abundance scatter (i.e. Si in PJ 5). These behaviours are also seen in other elements in a few other PJ clusters, as discussed in Section 4. It is not necessarily clear why there is such a discrepancy

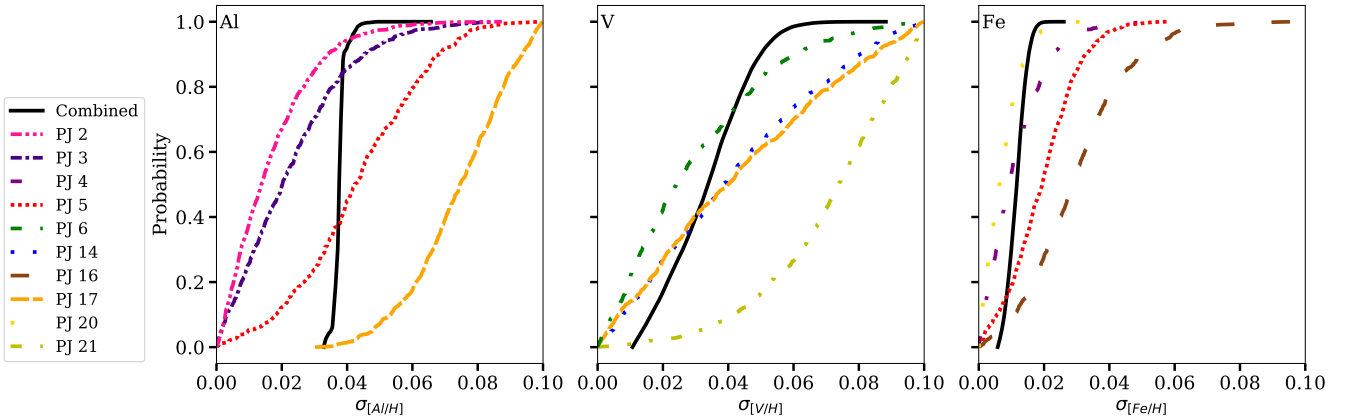


Figure 9. A summary plot of the cumulative posterior distribution functions for the intrinsic abundance scatter in Al, V, and Fe in a selection of chemically-tagged birth clusters from Price-Jones et al. (2020) that we study. In each panel, the black curve represents the cumulative posterior distribution function of the combined clusters. The subsequent curves in each panel represent the clusters that have the maximum and minimum upper limits in each element, as well as those that have upper limits that are approximately 33% and 66% of the way between the minimum and maximum upper limits. The 95% upper limits for each PJ birth cluster are reported in Table 4.

Table 4. The 95% upper limits on the constrained intrinsic abundance scatter for the 15 APOGEE elements for the PJ clusters that we analyze. A dashed entry indicates that not enough data is available for the element in question after we complete the masking and uncertainty considerations.

	PJ 2	PJ 3	PJ 4	PJ 5	PJ 6	PJ 9	PJ 10	PJ 11	PJ 12
C	0.033	0.017	0.026	0.043	0.017	0.049	0.028	0.026	0.048
N	0.093	0.059	0.053	0.047	0.03	0.075	0.059	0.067	0.065
O	0.043	0.063	0.062	0.068	0.02	0.034	0.029	0.041	0.045
Na	0.094	-	-	0.096	0.094	0.087	0.096	0.092	0.095
Mg	0.04	0.038	0.07	0.059	0.033	0.049	0.061	0.042	0.039
Al	0.04	0.055	0.094	0.088	0.047	0.085	0.078	0.073	0.063
Si	0.04	0.037	0.038	0.082	0.034	0.051	0.06	0.034	0.042
S	0.096	0.086	0.089	0.093	0.084	0.085	0.079	0.09	0.078
K	0.087	0.084	0.093	0.083	0.084	0.086	0.084	0.087	0.095
Ca	0.04	0.034	0.05	0.061	0.028	0.067	0.046	0.05	0.042
Ti	0.055	0.069	0.088	0.087	0.042	0.079	0.06	0.06	0.075
V	0.093	0.077	0.093	0.097	0.073	0.095	0.089	0.09	0.093
Mn	0.062	0.03	0.049	0.059	0.024	0.035	0.026	0.035	0.062
Fe	0.023	0.023	0.027	0.038	0.022	0.03	0.028	0.022	0.028
Ni	0.043	0.04	0.048	0.078	0.037	0.063	0.038	0.042	0.046

	PJ 14	PJ 15	PJ 16	PJ 17	PJ 18	PJ 19	PJ 20	PJ 21	Combined
C	0.024	0.033	0.059	0.048	0.032	0.043	0.031	0.044	0.019
N	0.06	0.049	0.091	0.077	0.045	0.089	0.047	0.089	0.043
O	0.037	0.051	0.05	0.088	0.059	0.044	0.035	0.083	0.029
Na	0.093	0.095	0.092	0.092	-	0.098	0.093	0.097	0.085
Mg	0.034	0.072	0.059	0.082	0.047	0.07	0.03	0.085	0.043
Al	0.048	0.043	0.059	0.097	0.058	0.058	0.044	0.097	0.054
Si	0.079	0.052	0.061	0.058	0.06	0.078	0.027	0.091	0.034
S	0.095	0.086	0.094	0.088	0.096	0.089	0.083	0.097	0.085
K	0.092	0.086	0.093	0.093	0.087	0.088	0.085	0.094	0.085
Ca	0.037	0.035	0.093	0.09	0.071	0.069	0.051	0.091	0.043
Ti	0.041	0.049	0.093	0.092	0.05	0.068	0.045	0.085	0.054
V	0.089	0.092	0.094	0.093	0.08	0.091	0.078	0.098	0.084
Mn	0.047	0.05	0.064	0.048	0.044	0.038	0.019	0.075	0.021
Fe	0.04	0.028	0.058	0.045	0.029	0.044	0.017	0.054	0.021
Ni	0.046	0.047	0.064	0.045	0.041	0.062	0.031	0.094	0.04

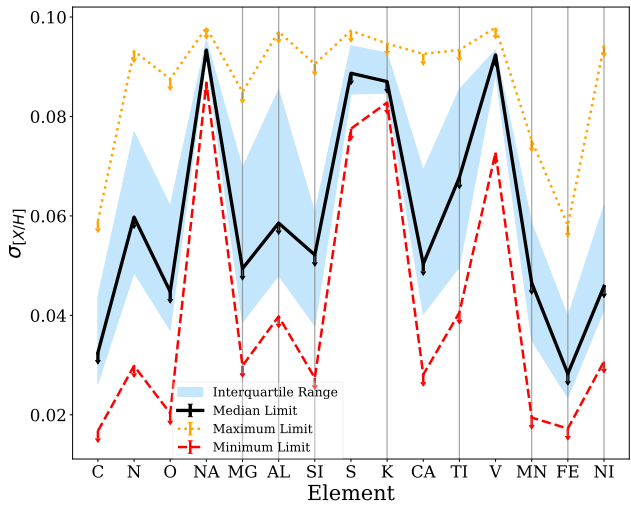


Figure 10. A summary plot of the constraints that we obtain for each element X in all of the chemically-tagged birth clusters. The median constraint on each element across the birth clusters is represented by the black arrows, connected by the solid black line for ease of visualization. The maximum constraint on each element is represented by the orange arrows, connected by the dotted orange line and the minimum constraint on each element is represented by the red arrows, connected by the dashed red line. The elements that were used by [Price-Jones et al. \(2020\)](#) to group these birth clusters are highlighted by the vertical grey lines.

in homogeneity between different elements in different clusters, however we will discuss potential reasons here.

One explanation could be that there is some aspect of the spectra that we are not taking into account in our modeling of these elements. There are several factors that could invalidate our assumption that non-elemental influences on the spectra can be modeled as a one-dimensional function of effective temperature. This could potentially be used to explain some of the weaker upper limits that we obtain and the apparent abundance scatter in some of the elements in the birth clusters discussed in Section 4. For example, there may be systematic uncertainties in these clusters that cannot be modeled as a smooth function of initial stellar mass, there may be mixing effects that we are not considering (such as deep mixing which can change the surface abundances of stars), or there may be other real-world complications that we are not modelling properly in our forward simulations, such as the existence of a binary companion (with mass transfer between binary companions resulting in spectral scatter). Such effects would be difficult to correct by any method (B16). As another example, stars can have a variety of initial rotation velocities, which can result in differences in the spectra of younger cluster members that cannot be modelled as a function of initial stellar mass ([Nielsen et al. 2013](#)). Initial velocity differences may also present complications, since they can result in present-day spectral scatter in the case that they brought about different mixing histories in the past. This will result in altered surface abundances of elements such as C and N ([Pinsonneault et al. 1990](#); [Meynet & Maeder 2002](#)).

For the most part, we circumvent these effects by examining giant stars. For example, cooler stars with deep convective zones present with stronger magnetic fields, and as such they lose angular momentum faster as a result of stellar winds ([Nielsen et al. 2013](#)), making our choice of using red giant stars with deep convective zones in a temperature range of $4000 \text{ K} \leq T_{\text{eff}} \leq 5000 \text{ K}$ beneficial.

However, different viewing angles will still result in spectral scatter. For the method in B16 to work for every stellar type, the $v \sin i$ of each star would need to be deduced prior to the performance of the forward simulations. Again, the fact that we study giant stars here should negate this effect, since their rotational velocities are small (B16), but perhaps the role of this effect needs to be considered more thoroughly in order to fully characterize the chemical homogeneity of these clusters. Specifically, perhaps the positions of the member stars of these chemically-tagged birth clusters in the Galaxy are increasing the importance of the effects of initial rotational velocities and viewing angles. These positions could have an important impact on their degree of chemical homogeneity, given that the members of each birth cluster are scattered across the Galactic disc, with each member having entirely different Galactic coordinates relative to their corresponding group members.

It is also possible that we are in fact modeling these clusters in a robust way already and that these clusters actually display signs of chemical inhomogeneity. There are many examples of effects that can cause present-day chemical abundances to be inhomogeneous, but sources of initial inhomogeneity are less obvious. However, perhaps the way in which stars are born can offer some insight into the reasoning for this effect. As stated in Section 1, most stars are born in birth clusters, which form in the collapse of a giant molecular cloud, and the two predictions for methods by which initial chemical homogeneity occurs is that the progenitor gas cloud was uniformly mixed in critical elements before stars began to form, or a few high mass stars may have formed soon after the development of the cloud, enriching the cloud in a uniform way ([Quillen 2002](#)). So, perhaps the progenitor clouds for these clusters were not well-mixed, or perhaps their high-mass stars formed after most of their low-mass stars ([Freeman & Bland-Hawthorn 2002](#)).

Additionally, there are numerous other effects that may result in different levels of chemical homogeneity in different elements, which could explain why some individual elements in some clusters look more like they have intrinsic abundance scatter than other elements in the same cluster. For example, planet formation can affect the chemical composition of stars ([Liu et al. 2019](#)). Refractory elements in the proto-stellar nebula, for example C, N, O, Si, S, Fe, and Ni ([Thiabaud et al. 2014](#)), which are elements that we analyze, may have been locked up in early-forming terrestrial planets, causing the gas left over for star formation and therefore the gas within the stars themselves to have reduced abundances of these refractory elements. On the other hand, early planetary infall into stars could increase the abundances of refractory elements in these stars ([Liu et al. 2019](#)). These selective planetary-forming elements could explain why some elements in each cluster display chemical homogeneity and some elements do not. Further investigation would need to be done to prove this, but a potential explanation for why chemical homogeneity is more apparent PJ 6 than PJ 5, for example, is that perhaps planets were more prevalent in PJ 5 before the members of this birth cluster became dispersed across the Galactic disc, relative to PJ 6.

Finally, elements like Na, Mg, V, and Mn can show a significant gradient in abundance with T_{eff} and $\log g$ due to non-LTE effects, changes of chemical abundances due to stellar evolutionary stage, and analysis systematics such as the blending of absorption lines; elements with a small number of lines, like Mn, are likely to be affected by this ([Casamiquela et al. 2020](#)). This could be a potential explanation for the inhomogeneity that we see in Mg in PJ 4 or Mn in PJ 18 and PJ 19, for example.

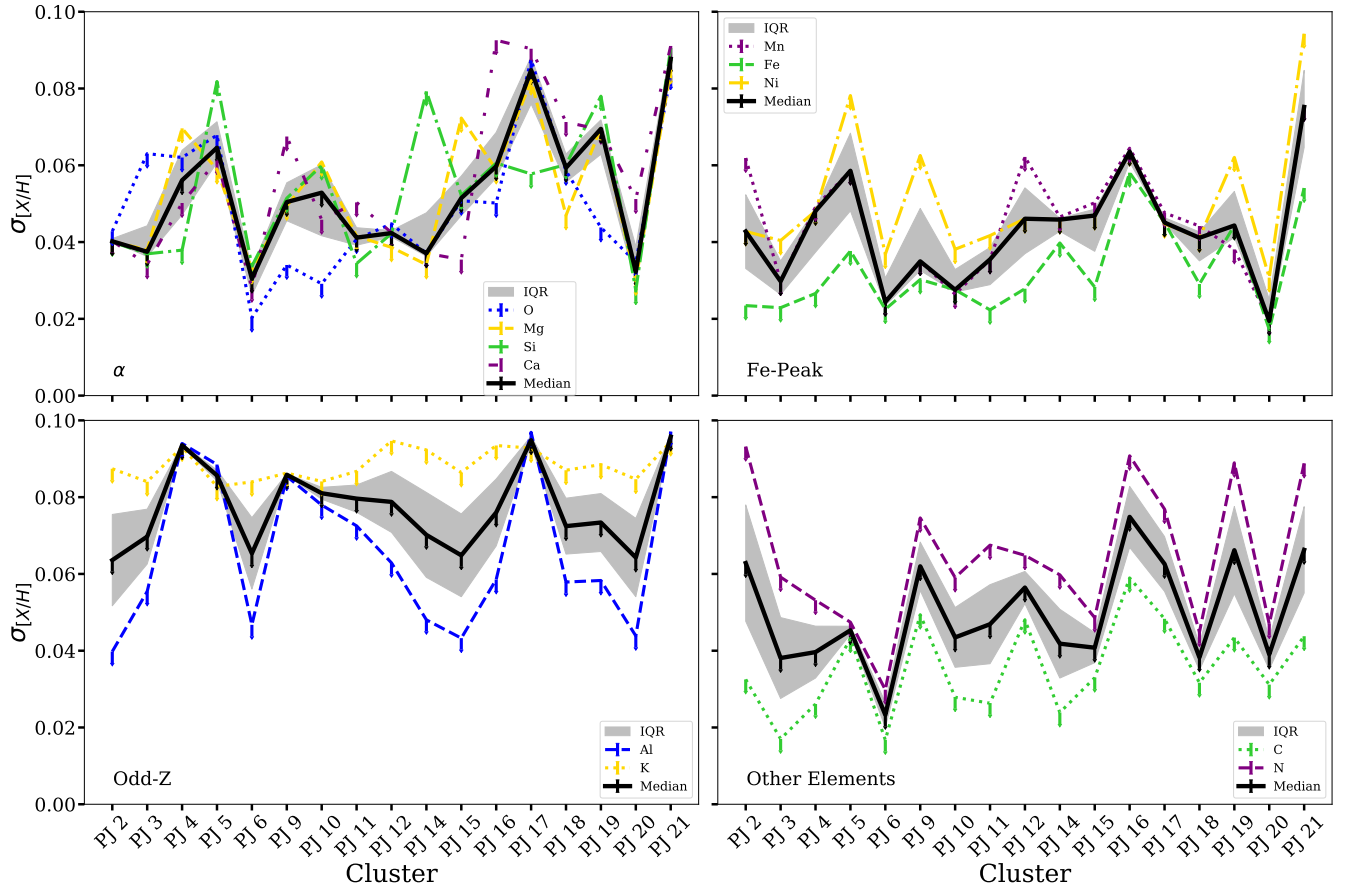


Figure 11. A summary plot of the constraints that we obtain for each chemically-tagged birth cluster, broken up into different elemental groupings. The constraints on some of the α -elements are shown in the top left panel, where the constraints on O are represented by the blue arrows, connected by the dotted blue line, the constraints on Mg are represented by the yellow arrows, connected by the dashed yellow line, the constraints on Si are represented by the green arrows, connected by the dot-dashed green line, and the constraints on Ca are represented by the purple arrows, connected by the dot-dot-dashed purple line. The constraints on the Fe-peak elements are shown in the top right panel, where the constraints on Mn are represented by the purple arrows, connected by the dotted purple line, the constraints on Fe are represented by the green arrows, connected by the dashed green line, and the constraints on Ni are represented by the yellow arrows, connected by the dot-dashed yellow line. The constraints on some of the odd-Z elements are shown in the bottom left panel, where the constraints on Al are represented by the blue arrows, connected by the dashed blue line, and the constraints on K are represented by the yellow arrows, connected by the dotted yellow line. Finally, the constraints on C and N are shown in the bottom right panel, where the constraints on C are represented by green arrows, connected by the dotted green line, and the constraints on N are represented by the purple arrows, connected by the dashed purple line. In each panel, the medians of the constraints for the elements shown in each panel are represented by the black arrows, connected by the solid black line, and the interquartile ranges of the constraints for the elements shown in each panel are represented by the grey region. We exclude some of the elements with few pixels available for analysis from this figure (i.e. Na, S, Ti, and V).

5.2 Strong Constraints in Chemically-Tagged Birth Clusters

As alluded to in Section 4, in general, we obtain much stronger limits on the intrinsic abundance scatter in the PJ clusters than the OCCAM clusters, when comparing the combined limits on each element in the PJ clusters to the individual limits on each element in the OCCAM clusters. It is perhaps surprising that we obtain such strong limits on the intrinsic abundance scatter of the chemically-tagged birth clusters compared to the open clusters, especially when considering the fact that the open clusters are still gravitationally bound while the birth cluster members are no longer in close proximity to each other. However, these results are consistent with the analysis completed by Price-Jones et al. (2020). In Price-Jones et al. (2020), each chemically-tagged birth cluster was found to be exceptionally chemically homogeneous when compared to a chemically similar population. Each chemically similar population consisted of

a selection of stars across APOGEE that have $[\text{Fe}/\text{H}]$ and $[\text{Mg}/\text{Fe}]$ within 0.05 dex of the median value of those abundances in each birth cluster.

While the constraints on the intrinsic abundance scatter in the PJ birth clusters are much stronger than those in the OCCAM open clusters that we test, we discussed in Section 5.1 above that there are some signs of potential chemical inhomogeneity in some of the elements of some of these birth clusters. However, despite all of these potential factors that could be resulting in small amounts of chemical inhomogeneity, we are still able to obtain strong combined constraints on nearly every element that has enough pixels available for analysis. The fact that we see minimal levels of chemical inhomogeneity and in fact are mostly able to obtain very strong constraints is a testament to the power of this method of constraining abundance scatter - even though the member stars of these chemically-tagged birth clusters are scattered across the Galactic disc and are no longer

related to each other in an obvious way, we are still able to constrain their chemical homogeneity in a very robust way.

Additionally, from examining Figure 10 in Section 4, we can see that the maximum constraints in each element are still generally well below 0.1 dex, excluding those elements that do not have many pixels available for analysis. It is clear that the minimum constraints on each element are generally very strong, with those for C and Fe being the strongest. Similar conclusions can be made from examining Figure 11 in Section 4 for various constraints in each birth cluster. In excluding most of the elements with few pixels available for analysis from these figures, it is clear that the most of the elements in the majority of the birth clusters have very strong constraints.

5.3 Implications for Chemical Tagging

In B16, it was found that the results of this study held promise for the method of chemical tagging, as a result of the fact that tight constraints were found for each cluster studied. The somewhat disparate results of our current study, with a few elements in some of the clusters that we study displaying intrinsic abundance scatter, may result in different implications for chemical tagging studies. Here we will discuss the potential implications from the elements and clusters that display chemical homogeneity, those from the elements and clusters that display chemical inhomogeneity, and the implications from the tight limits that we are able to obtain on the chemically-tagged birth clusters.

5.3.1 Implications from Chemically Homogeneous Clusters

B16 cites several advantages and disadvantages for the developed method we use compared to the traditional method of determining the chemical homogeneity of open clusters through derived abundances. These advantages and disadvantages and the implications for chemical tagging certainly hold for several of the PJ clusters and are worth discussing here.

First, this method of obtaining tight upper limits on the chemical abundance scatter in chemically-tagged birth clusters allows us to avoid complications introduced by systematic uncertainties in the chemical abundances. In traditional chemical homogeneity studies, these systematic uncertainties appear as a result of the fact that measuring consistent abundances across various stellar types can be challenging. For example, inconsistencies can result from ambiguities in the elemental line list, one-dimensional radiative transfer, and inconsistencies with the assumptions of local thermodynamic equilibrium (Ness et al. 2015). The aspect of these effects that can be used to the advantage of the method in B16 is that the uncertainties created by these effects can be modelled as smooth function of initial stellar mass, and therefore T_{eff} , the foundation of the model we use. Additionally, since this method does not prescribe any behaviour to the overall T_{eff} trends of the stellar spectra used, we directly avoid the uncertainties stemming from all of these effects.

A common problem for chemical tagging studies is the inhomogeneity of present-day chemical abundances in cluster members due to stellar-evolutionary effects on surface abundances, such as deep mixing, gravitational settling, or atomic diffusion (Dotter et al. 2017). These effects can alter the surface abundance of stars in a way that is not well understood, and therefore they are difficult to model. However, the consequences of these effects are predominantly deterministic functions of stellar mass. Once again, our method of modeling stellar spectra as a one-dimensional function of initial

stellar mass allows us to constrain the *initial* abundance scatter in the chemically-tagged birth clusters, as opposed to the present-day scatter (B16).

Finally, since this technique makes use of forward simulations and ABC, realistic complications seen in the observed spectra can be taken into account in these simulations. These effects include, for example, correlated spectral noise and uncertainties that result from the applied continuum normalization (B16).

5.3.2 Implications from Chemically Inhomogeneous Clusters

The potential evidence of chemical inhomogeneity in some of the elements in a few of the PJ clusters may not spell the end for chemical tagging studies. Previously, it was thought that chemical homogeneity was a requirement for chemical tagging (Freeman & Bland-Hawthorn 2002). However, as discussed in Section 1, Casamiquela et al. (2020) studied the Hyades, Praesepe, and Ruprecht 147 open clusters. They found that there was a certain level of chemical inhomogeneity in each of these clusters, however, it was still possible to distinguish the chemical signature of Ruprecht 147 from the Hyades and Praesepe. Perhaps this is an indication that the requirements for chemical tagging can be relaxed - while chemical homogeneity is required for chemical tagging, the level of homogeneity required may not need to be as strong as previously thought.

Regardless of whether or not these clusters are truly homogeneous, these results still allow for a greater understanding of the chemical and dynamical history of the Galactic disc. If clusters like PJ 5, for example, are truly inhomogeneous, this may indicate a lack of uniformity that is usually assumed in the early stages of the formation of the Galaxy.

5.3.3 Implications from Constraining Chemically-Tagged Birth Clusters

Our ability to strongly constrain the intrinsic abundance scatter in the majority of the chemically-tagged birth clusters from Price-Jones et al. (2020) indicates great promise for chemical tagging studies. As stated in Section 1, the ability to reconstruct star clusters that have been dispersed across the Galactic disc will reveal crucial information about the chemical and dynamical evolution of the Galactic disc. By constraining the levels of chemical homogeneity within reconstructed star clusters, we are able to have a greater understanding of the conditions under which these groups and the stars within these groups formed, including the abundances of certain elements that were present at the time of their formation, as well as which elements were key to their formation.

Additionally, in finding that the levels of chemical homogeneity in these chemically-tagged birth clusters are stronger than those in various open clusters, consistent with findings in Price-Jones et al. (2020), we have further solidified the association of these chemically-tagged stars as members of the same birth clusters. This is encouraging for future chemical tagging studies and can also allow us to study these specific chemically-tagged birth clusters in more detail. For example, we can more closely study the migration patterns of these stars as they separated from their common formation sites and travelled across the Galactic disc.

6 CONCLUSION

In conclusion, we constrained the initial abundance spread in several blindly chemically-tagged birth clusters found by Price-Jones

et al. (2020). We determined these constraints using a method first developed by B16, whereby we modeled the stellar spectra as a one-dimensional function of initial stellar mass, performed quadratic fits, and produced cumulative distributions of the uncertainty-normalized fit residuals. We completed forward modeling of the spectra by generating synthetic APOGEE spectra using the POLYNOMIAL SPECTRAL MODELING code Rix et al. (2016) and a variety of values of intrinsic abundance scatter, drawn from a uniform prior of 0 to 0.1 dex. We compared the synthetic spectra to the observed spectra via Approximate Bayesian Computation through the use of two summary statistics: the Kolmogorov-Smirnov distance (D_n) and a covariance matrix statistic ($|\Delta\text{Cov}_{ij}|$). We produced the cumulative posterior distribution function of the values of intrinsic abundance scatter of the simulations that are the closest to the data and we obtained upper limits on the intrinsic abundance scatter at 95% confidence. We tested this method using the open clusters M67, NGC 6819, NGC 7789, and NGC 6791, data for which we obtained from the Open Cluster Chemical Analysis and Mapping survey (Donor et al. 2018). For M67 and NGC 6819, which were also studied in B16, we find that we obtain similar results on the intrinsic abundance scatter of these clusters, within uncertainties introduced by differences in our methods.

In general, we find very strong limits on the intrinsic abundance scatter of the chemically-tagged birth clusters, with strong constraints ($\lesssim 0.5$ dex at 95% confidence) on the abundance scatter in every element except for those which have very few pixels available for analysis. While we find some evidence for a small amount of chemical inhomogeneity in some of the elements in a few of the PJ birth clusters, we are still able to obtain stronger limits on the intrinsic abundance scatter of these clusters compared to the OC-CAM open clusters, consistent with findings by Price-Jones et al. (2020).

These results hold great promise for the method of chemical tagging. We find that most of the elements in most of the chemically-tagged birth clusters have strong levels of chemical homogeneity. For the few that show some intrinsic abundance scatter, it may be possible to relax the constraints on the level of chemical homogeneity that is required for chemical tagging and distinguish the chemical signatures of different stellar groups, as found by Casamiquela et al. (2020). Regardless, by strongly constraining the levels of chemical homogeneity within reconstructed stellar birth clusters, we are able to further solidify the association of these chemically-tagged stars as birth clusters and to have a clearer understanding of the chemical and dynamical history of the Galactic disc.

DATA AVAILABILITY

The data upon which this research is based is publicly available as part of SDSS-IV's DR14 data release (<https://www.sdss.org/dr14>).

ACKNOWLEDGEMENTS

The authors acknowledge the land on which the University of Toronto operates. For thousands of years it has been the traditional land of the Huron-Wendat, the Seneca, and the Mississaugas of the Credit River, and it is home to many Indigenous people from across Turtle Island. The authors are grateful to have the opportunity to work on this land. The authors also acknowledge the land on which the Apache Point Observatory is located, the traditional land of

the Pueblo of Sandia, the Navajo, and the Apache. The authors are grateful to have access to the data collected on this land.

This research received financial support from NSERC (funding reference numbers RGPIN-2015-05235 & RGPIN-2020-04712), an Ontario Early Researcher Award (ER16-12-061), and from the Canada Research Chair program. NPJ received support from an Alexander Graham Bell Canada Graduate Scholarship-Doctoral from the Natural Sciences and Engineering Research Council of Canada.

Funding for the Sloan Digital Sky Survey IV has been provided by the Alfred P. Sloan Foundation, the U.S. Department of Energy Office of Science, and the Participating Institutions. SDSS-IV acknowledges support and resources from the Center for High-Performance Computing at the University of Utah. The SDSS web site is www.sdss.org.

REFERENCES

Abolfathi B., et al., 2018, *ApJS*, **235**, 42
 Alam S., et al., 2015, *ApJS*, **219**, 12
 Allen L., et al., 2006, The Structure and Evolution of Young Stellar Clusters ([arXiv:astro-ph/0603096](https://arxiv.org/abs/astro-ph/0603096))
 Alvarez R., Plez B., 1998, *A&A*, **330**, 1109
 Bailer-Jones C. A. L., Rybizki J., Fouesneau M., Mantelet G., Andrae R., 2018, *AJ*, **156**, 58
 Blanco-Cuaresma S., Soubiran C., Heiter U., 2014, in EAS Publications Series. pp 133–136 ([arXiv:1507.06294](https://arxiv.org/abs/1507.06294)), doi:10.1051/eas/1567023
 Blanton M. R., et al., 2017, *AJ*, **154**, 28
 Bovy J., 2016, *AJ*, **817**, 49 (B16)
 Bovy J., et al., 2014, *ApJ*, **790**, 127
 Casamiquela L., Tarricq Y., Soubiran C., Blanco-Cuaresma S., Jofré P., Heiter U., Tucci Maia M., 2020, *A&A*, **635**, A8
 Cutri R. M., et al., 2003, 2MASS All Sky Catalog of point sources.
 De Silva G. M., Sneden C., Paulson D. B., Asplund M., Bland-Hawthorn J., Bessell M. S., Freeman K. C., 2006, *AJ*, **131**, 455–460
 De Silva G. M., Freeman K. C., Asplund M., Bland-Hawthorn J., Bessell M. S., Collet R., 2007, *AJ*, **133**, 1161–1175
 De Silva G. M., Freeman K. C., Bland-Hawthorn J., 2009, in Andersen J., Nordströra m B., Bland -Hawthorn J., eds, IAU Symposium Vol. 254, The Galaxy Disk in Cosmological Context. pp 133–138, doi:10.1017/S1743921308027506
 Donor J., et al., 2018, *AJ*, **156**, 142
 Dotter A., Conroy C., Cargile P., Asplund M., 2017, *ApJ*, **840**, 99
 Ester M., Kriegel H.-P., Sander J., Xu X., et al., 1996, in Kdd. pp 226–231
 Feng Y., Krumholz M. R., 2014, *Nature*, **513**, 523
 Freeman K., Bland-Hawthorn J., 2002, *Annu. Rev. Astron. Astrophys.*, **40**, 487–537
 Gaia Collaboration et al., 2018, *A&A*, **616**, A1
 García Pérez A. E., et al., 2016, *AJ*, **151**, 144
 Gilroy K. K., Brown J. A., 1991, *ApJ*, **371**, 578
 Girardi L., 2016, *ARA&A*, **54**, 95
 González Hernández J. I., Bonifacio P., 2009, *A&A*, **497**, 497–509
 Gray D. F., 1982, *ApJ*, **261**, 259
 Gunn J. E., et al., 2006, *AJ*, **131**, 2332
 Hinkle K., Wallace L., Livingston W., 1995, *PASP*, **107**, 1042
 Hogg D. W., Bovy J., Lang D., 2010, Data analysis recipes: Fitting a model to data ([arXiv:1008.4686](https://arxiv.org/abs/1008.4686))
 Holtzman J. A., et al., 2015, *AJ*, **150**, 148
 Holtzman J. A., et al., 2018, *AJ*, **156**, 125
 Ivezić Z., Connolly A. J., VanderPlas J. T., Gray A., 2014, Statistics, Data Mining, and Machine Learning in Astronomy: A Practical Python Guide for the Analysis of Survey Data
 Lada C. J., Lada E. A., 2003, *ARA&A*, **41**, 57
 Leung H. W., Bovy J., 2019a, *MNRAS*, **483**, 3255
 Leung H. W., Bovy J., 2019b, *MNRAS*, **489**, 2079

Liu F., Yong D., Asplund M., Ramírez I., Meléndez J., 2016, [MNRAS](#), **457**, 3934

Liu F., Asplund M., Yong D., Feltzing S., Dotter A., Meléndez J., Ramírez I., 2019, [A&A](#), 627, A117

Majewski S. R., et al., 2017, [AJ](#), 154, 94

Massey Jr. F. J., 1951, [Journal of the American Statistical Association](#), 46, 68

McKee C. F., Tan J. C., 2002, [Nature](#), **416**, 59

Mészáros S., et al., 2013, [AJ](#), **146**, 133

Meynet G., Maeder A., 2002, [A&A](#), **390**, 561

Ness M., Hogg D. W., Rix H.-W., Ho A. Y. Q., Zasowski G., 2015, [ApJ](#), 808, 16

Nidever D. L., et al., 2015, [AJ](#), **150**, 173

Nielsen M. B., Gizon L., Schunker H., Karoff C., 2013, Measuring Stellar Rotation Periods with Kepler. p. 137

Pancino E., Carrera R., Rossetti E., Gallart C., 2010, [A&A](#), **511**, A56

Pinsonneault M. H., Kawaler S. D., Demarque P., 1990, [ApJS](#), **74**, 501

Poovveli V. J., et al., 2020, arXiv e-prints, p. [arXiv:2009.06777](#)

Price-Jones N., et al., 2020, [MNRAS](#),

Quillet A. C., 2002, [AJ](#), 124, 400–403

Rix H.-W., Ting Y.-S., Conroy C., Hogg D. W., 2016, [ApJ](#), **826**, L25

Skrutskie M. F., et al., 2006, [AJ](#), **131**, 1163

Souto D., et al., 2018, [ApJ](#), **857**, 14

Souto D., et al., 2019, [ApJ](#), **874**, 97

Spina L., Meléndez J., Casey A. R., Karakas A. I., Tucci-Maia M., 2018, [ApJ](#), **863**, 179

Sunnåker M., Busetto A. G., Numminen E., Corander J., Foll M., Dessimoz C., 2013, [PLoS Comput Biol](#), 9, 1

Thiabaud A., Marboeuf U., Alibert Y., Cabral N., Leya I., Mezger K., 2014, [A&A](#), **562**, A27

Ting Y.-S., Conroy C., Rix H.-W., 2015, [ApJ](#), 816, 10

Wright E. L., et al., 2010, [AJ](#), **140**, 1868

de Medeiros J. R., Da Rocha C., Mayor M., 1996, [A&A](#), **314**, 499

This paper has been typeset from a $\text{\TeX}/\text{\LaTeX}$ file prepared by the author.